

Antibody binding reports spatial heterogeneities in cell membrane organization

Daniel P. Arnold^a, Yaxin Xu^a, and Sho C. Takatori^{a,1}

^aDepartment of Chemical Engineering, University of California, Santa Barbara, Santa Barbara, CA 93106

This manuscript was compiled on November 23, 2022

The mammalian plasma membrane regulates cellular interactions with the extracellular environment through a dense assembly of membrane glycoproteins and glycolipids. Although the spatial organization of the cell surface glycocalyx is critical for mediating the binding of ligands, receptors, and macromolecules on the plasma membrane, we currently do not have the methods to quantify the spatial heterogeneities on live cell surfaces. In this work, we engineer molecular antigen sensors that act as a direct reporter of live cell surface crowding heterogeneities with nanometer spatial resolution. By quantifying the effective binding affinity of IgG monoclonal antibodies to our antigen sensors on reconstituted and live cells, we provide a biophysical understanding of the molecular-to-mesoscale spatial organization of the glycocalyx. We find that the antigen location strongly influences the IgG binding on the red blood cell membrane, with the strongest gradients occurring within a few nanometers of the membrane. We develop an analytical theory and coarse-grained molecular dynamics simulations to corroborate our results, and combine surface proteomics with our simulations and theory for an in-silico reconstruction of the red blood cell surface. We also show that the effective binding affinity above raft-like domains is much higher than that of the bulk membrane on human cancer cells, suggesting that raft-like domains exclude membrane proteins with bulky extracellular domains. Our facile and high-throughput method to quantify spatial crowding heterogeneities on live cell membranes may facilitate monoclonal antibody design and provide a mechanistic understanding of plasma membrane biophysical organization.

Plasma membrane | Glycocalyx | Ligand binding | Antibodies | Cell surface crowding | Proteomics | Molecular dynamics

Physical crowding of the cell surface glycocalyx has been shown recently to alter the biophysical properties of membranes in a manner that significantly impacts cell function. These alterations include membrane bending, stretching, and fission on reconstituted lipid bilayers (1–5), as well as tubulation and fission in the plasma membranes of cultured cells (6, 7). In addition to inducing membrane deformation, cell surface crowding also modulates the physical accessibility of surface receptors to large soluble ligands and macromolecules (8). Experiments on reconstituted membranes with grafted synthetic polymers or purified proteins further confirm a decrease in protein binding affinity with increasing grafting density (9–12). Most clinical monoclonal antibody drugs that rely on direct effector-cell activity are known to target antigen receptors that are buried deep inside the glycocalyx, often within 10 nm from the membrane surface (13, 14), suggesting that their effectiveness may be highly dependent upon crowding near the receptor. However, there are currently no methods to characterize the piconewton-scale forces generated by the crowding of ~ 10 nm cell surface proteins (15).

In addition to surface-orthogonal variations, the mammalian plasma membrane composition is also laterally-

heterogeneous, with nanometer-scale protein and lipid clusters forming and dissipating on sub-second timescales (15, 16). In giant plasma membrane vesicles (GPMVs) isolated from cells, Levental et al. (17–19) showed that raft-like membrane microdomains exclude most transmembrane proteins, suggesting that raft-like domains on cells are lipid-rich and protein-poor relative to the bulk regions of the membrane. Given the lateral and membrane-orthogonal heterogeneity of the glycocalyx, a complete picture of the crowding profile requires three-dimensional (3D) characterization.

While techniques like electron microscopy enable nanometer-scale characterization of the plasma membrane, the preparation process is destructive (20), leaving a need for appropriate molecular probes to study these complex, dynamic systems *in-vivo* (15). Recently, Houser et al. (21) quantified the surface pressures on reconstituted crowded membranes by measuring the separation distance between FRET fluorophores that stretch due to steric interactions within the brush. The stretching distance in polymer brushes depends weakly on surface density, as height scales with chain density according to $h \sim n^{1/3}$ in the brush regime (22, 23) and follows even weaker scaling in the mushroom regime (24). Therefore, the technique may lose accuracy at the crowding densities observed in physiological surface densities on live cells.

In this work, we develop synthetic antigen sensors with precise spatial localization and measure the binding affinity of complementary immunoglobulin G (IgG) monoclonal antibodies in these local crowding environments. We leverage a technique developed recently by Takatori and Son et al. (25), in which a macromolecular probe is introduced to the extracellular side of a plasma membrane to quantify the local osmotic pressure posed by the crowded cell surface via a reduction

Significance Statement

The mammalian cell surface is decorated with a protective “shield” of membrane proteins and sugars that enables cells to mediate interactions with the extracellular environment. The precise spatial distribution of the proteins and sugars are critical for cell function, but we currently do not have the techniques to quantify the spatial heterogeneities on the cell membrane surface. In this work, we develop a method to quantify the spatial organization of the cell surface by engineering molecular antigen sensors that act as a direct reporter of local macromolecular crowding.

D.P.A. and S.C.T. conceived of the study; all authors designed research; D.P.A. performed experiments; Y.X. performed simulations; S.C.T. supervised the study; and all authors wrote the paper.

The authors have no competing interests to declare.

¹To whom correspondence should be addressed. E-mail: stakatori@ucsb.edu

in effective binding affinity. We advance this technique by enabling spatial localization of the binding site to measure the membrane-orthogonal crowding heterogeneity on both reconstituted membranes and red blood cell (RBC) surfaces. We then reconstruct these systems in-silico, combining proteomics with molecular dynamics (MD) simulations and experiments to map RBC glycocalyx crowding with nanometer-scale spatial precision. Using targeted antigen probes, we expand our spatial resolution laterally, in the plane of the membrane, measuring differences in crowding between plasma membrane domains on live tumor cells. Our findings support the hypothesis that raft-like domains of native membranes exclude bulky proteins, consistent with the findings of Levental et al. on GPMVs (17–19). Our simple IgG binding assay to probe spatial heterogeneities on native cell membranes suggests an important role of structural complexities on glycocalyx organization.

Results

Synthetic antigen sensors report crowding heterogeneities with nanometer height resolution. The glycocalyx is heterogeneous in both composition and density, which vary as a function of distance from the membrane surface (henceforth “height”). Height heterogeneities in crowding can arise from variations in protein sizes (26–29) and also from polymer brush dynamics of disordered glycoproteins like mucins in the glycocalyx (6, 8, 30–32). To characterize the cell surface height heterogeneity, we developed a noninvasive synthetic antigen sensor that inserts into the lipid membrane using a cholesterol tag conjugated to a polyethylene glycol (PEG) linker and a fluorescein isothiocyanate (FITC) fluorophore (Fig. 1A). We developed a family of cholesterol-PEG-FITC sensors with varying PEG linker lengths to adjust the height of the FITC antigen presented above the membrane. After presenting the antigen sensors on the cell surface, we obtain the effective binding avidity of anti-FITC (α FITC) IgG antibody as a function of antigen height.

The PEG linker enables the FITC antigen to sample a distribution of heights above the membrane, while the mean height, $\langle h \rangle$, increases with the molecular weight of PEG. We used cell surface optical profilometry (CSOP) (33) to measure $\langle h \rangle$ of the FITC antigen for sensor linker lengths of 0.5 kDa PEG (PEG0.5k), 2k, 5k, and 10k using silica beads coated with a 1,2-dioleoyl-sn-glycero-3-phosphocholine (DOPC) supported lipid bilayer (SLB). We recovered the predicted increase in $\langle h \rangle$ with molecular weight (Fig. 1B), suggesting that the antigen is probing different crowding microenvironments as a function of linker length.

To validate that our different sensors are probing the height heterogeneities of a crowded membrane surface, we measured α FITC IgG binding to our antigen sensors on a reconstituted glycocalyx-mimetic PEG brush. Our reconstituted SLB on 4 μ m silica beads included 3% 1,2-dioleoyl-sn-glycero-3-phosphoethanolamine-N-[methoxy(polyethylene glycol)-2000] (DOPE-PEG2k) to act as a repulsive brush, with synthetic antigen sensors of a single type inserted into the outer membrane leaflet (see Materials and Methods). Beads were incubated in varying concentrations of fluorescently-labeled α FITC antibodies and allowed to reach equilibrium before fluorescence intensities of beads were collected via fluorescence microscopy. Intensities were fit to a Hill binding isotherm to calculate the dissociation constant K_D (see Supplementary Information).

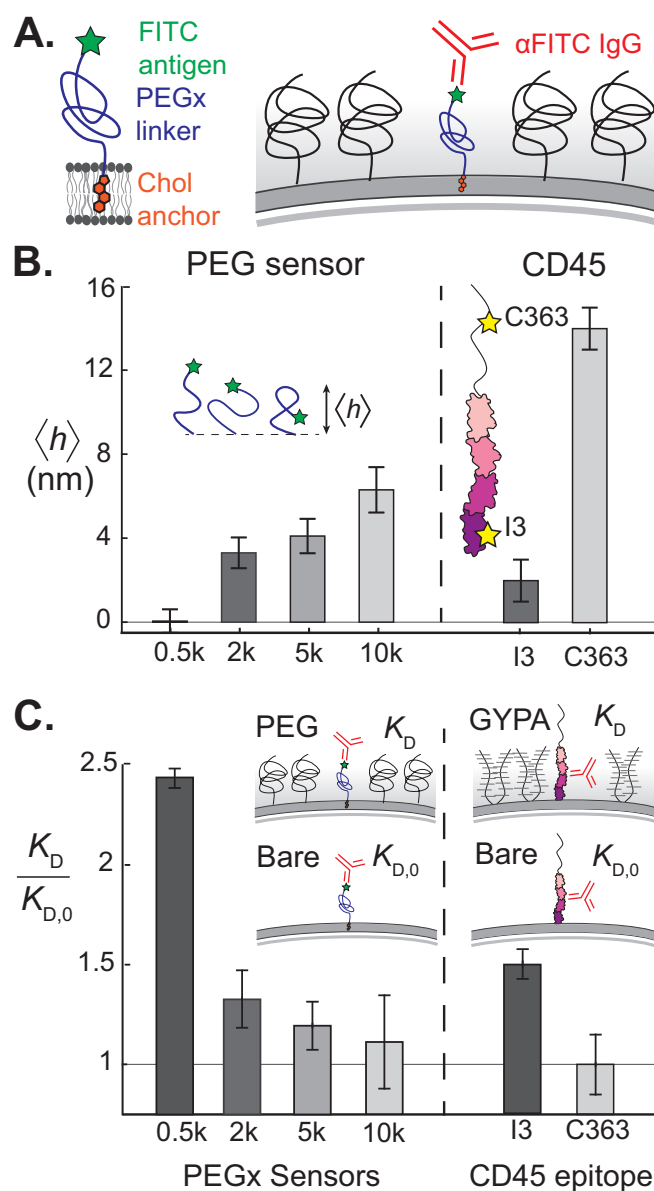


Fig. 1. Synthetic antigen sensors enable precise localization and measurement of IgG binding avidity on crowded membrane surfaces. (A) Cholesterol-PEG-FITC sensors insert into the membrane and present the FITC antigen at varying heights above the membrane, depending on the PEG linker length. Sensors are exogenously inserted into reconstituted or live plasma membranes, and α FITC IgG avidity is a direct reporter of local crowding. (B) (Left) Mean height $\langle h \rangle$ of synthetic antigen sensors increases as a function of PEG linker molecular weight, as measured by CSOP (33). (Right) Epitope heights of two different α CD45 antibodies, α I3 and α C363 on the transmembrane tyrosine phosphatase CD45 (33). (C) (Left) Dissociation constants of α FITC to the synthetic antigen sensors on a supported lipid bilayer, containing 3% DOPE-PEG2k as a surface crowder. Dissociation constants are normalized by the bare membrane value, $K_{D,0}$. (Right) Two α CD45 antibodies with distinct epitope heights experience a significant difference in normalized avidity on a reconstituted membrane crowded with a mucin-like glycoprotein, Glycophorin A (GYPA).

The ratio of K_D on the PEG-crowded SLB to that on a bare SLB with no PEG crowders, $K_D/K_{D,0}$, decreases toward unity as the average FITC height increases (Fig. 1C). The FITC antigen on our 10k antigen sensor samples the majority of its height distribution above the DOPE-PEG2k steric brush and has a α FITC binding avidity that is essentially unchanged from the bare membrane value. In contrast, the 0.5k antigen

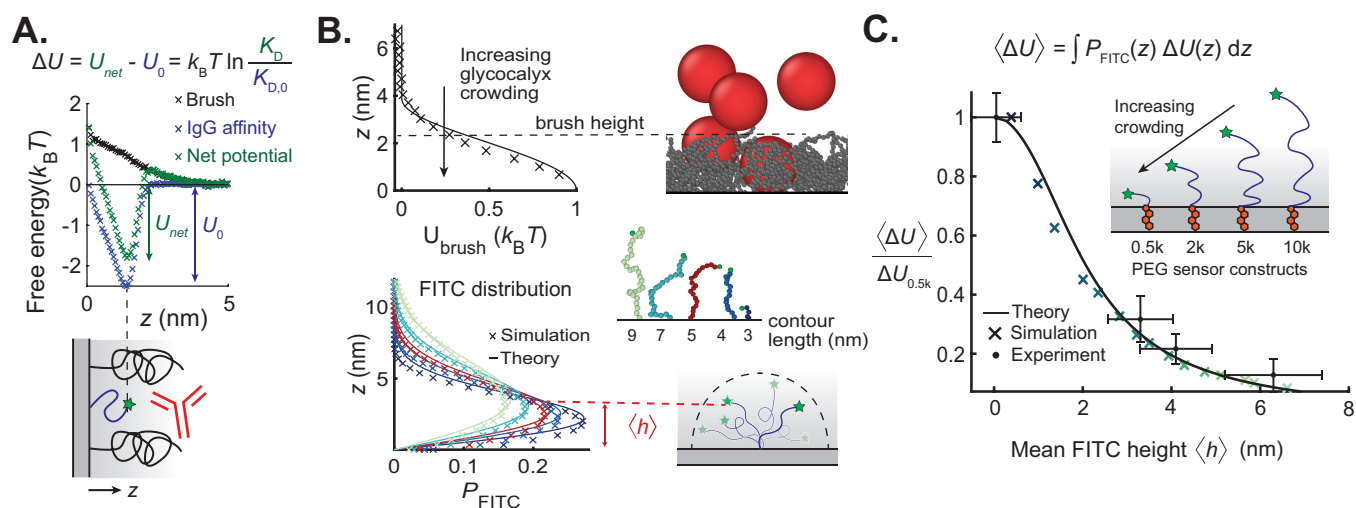


Fig. 2. The binding avidity of macromolecules on crowded surfaces is a direct reporter of the energetic penalty posed by the crowded surface. (A) Coarse-grained molecular dynamics (MD) simulations of the IgG free energy versus height above the surface. The observed IgG avidity (U_{net} , green) is a superposition of an attractive enthalpic binding potential (U_0 , blue) and a repulsive potential due to crowding polymers (ΔU , black). Therefore, the normalized dissociation constants from Fig. 1C report the local energy penalty of the crowded surface. (B) (Top left) MD simulations of repulsive crowding potential are re-plotted from Fig. 2A, with solid line indicating classical polymer brush theory (30). (Top right) Simulation snapshot of antibody (red) on polymer (gray) coated surface. Weighting the crowding potential by the FITC distribution yields a mean crowding potential $\langle \Delta U \rangle$ for a sensor of given $\langle h \rangle$. (Bottom left) FITC position probability distributions for different polymer contour lengths based on continuous Gaussian chain model (34) (curve) and MD simulations (crosses). (Bottom right) MD snapshots of sensors of different linker lengths and illustration of average height $\langle h \rangle$ of a fluctuating FITC antigen. (C) Antibody avidity data from Fig. 1c are re-plotted to report steric crowding energy as a function of the mean FITC antigen height from Fig. 1B (black circles). Energies are normalized by the smallest antigen sensor size, $\Delta U_{0.5k} = 0.9k_B T$. Theoretical prediction based on polymer brush theory (curve) agrees with experimental data and MD simulations (crosses).

sensor is buried deep inside the PEG brush and the accessibility of the FITC antigen is hindered by a factor of six (Fig. 1C). Our results are consistent with classical polymer brush theory, which predicts a monotonic decrease in brush monomer density with height (30) and a reduction in the effective adsorption energy of a globular protein onto a brush-coated surface (35).

Based on our results for synthetic sensors on a PEG surface, we hypothesized that the height-dependent avidity of IgG would also apply to protein antigens buried within a crowded surface of other membrane proteins. To investigate, we reconstituted an SLB containing 5% 1,2-dioleoyl-sn-glycero-3-[(N-(5-amino-1-carboxypentyl)iminodiacetic acid)succinyl] (DGS-NTA) and created a crowded surface of poly-histidine tagged glycoprotein, Glycophorin A (GYPA). Instead of synthetic antigen sensors, we tethered a dilute surface density of tyrosine phosphatase CD45 on the SLB among the crowded excess of GYPA. As a readout of GYPA crowding, we used α CD45 antibodies that target two different epitope sites: pan-CD45 I3 epitope on the first FN3 domain ($\langle h \rangle = 2.5$ nm), and R_B isoform epitope C363 on the upper mucin-like domain ($\langle h \rangle = 15$ nm). Using scaling arguments and the known glycosylation sequence of GYPA (36, 37) we estimate an average GYPA height of $\langle h \rangle = 12$ nm, so we expected the C363 epitope to explore uncrowded regions above the GYPA brush, while the I3 epitope to remain buried within the brush. Indeed, the relative avidities of α C363 and α I3 agree with this hypothesis, as $K_D/K_{D,0} \approx 1$ for α C363 while it is ≈ 1.5 for α I3 (Fig. 1C). The consistent correlation between increasing antigen height, $\langle h \rangle$, and decreasing dissociation constant, $K_D/K_{D,0}$, on both PEG and protein brushes confirms that antibody avidity is a robust metric of local crowding.

Macromolecular binding is a direct reporter of steric energies on crowded surfaces. In this section, we aim to obtain a direct

relation between the antibody binding avidity and the local steric free energy penalty of a crowded surface. We combine polymer brush theories with coarse-grained MD simulations to obtain a mechanistic understanding of our synthetic antigen sensors and their applicability on crowded membrane surfaces.

To characterize the energy profile on the membrane, we separately simulated free antibody insertion into a surface-tethered PEG2k brush and antibody binding to surface-tethered sensors to obtain the repulsive penalty associated with crowding, ΔU , (Fig. 2A), and the attractive binding potential, U_0 , respectively (see Materials and Methods). We invoke the theory of Halperin (35) and hypothesize that the effective antibody binding potential on a crowded interface, U_{net} , is a superposition of U_0 and ΔU . The bare membrane binding avidity reports the attractive enthalpic term $U_0 = k_B T \ln K_{D,0}$, so that the repulsive entropic energy penalty posed by the brush is given by

$$\Delta U = U_{net} - U_0 = k_B T \ln \frac{K_D}{K_{D,0}}. \quad [1]$$

The repulsive energy barrier of the brush, ΔU , is proportional to the osmotic pressure, Π , which scales with monomer volume fraction ϕ as $\Pi \sim \phi^{9/4}$ (24, 35). The Milner, Witten, and Cates (30) self-consistent field description of a polymer brush predicts a parabolic monomer distribution, so the potential ΔU follows a stretched parabolic profile (Fig. 2B, see Supporting Information for analytical form). Kenworthy et al. showed experimentally that the pressure between apposite membrane-tethered PEG brushes under compression varies with distance according to a profile derived from Milner theory (38). We therefore invoke this theory to describe the form of our PEG2k brush potential, which we verify using MD simulations (see Materials and Methods).

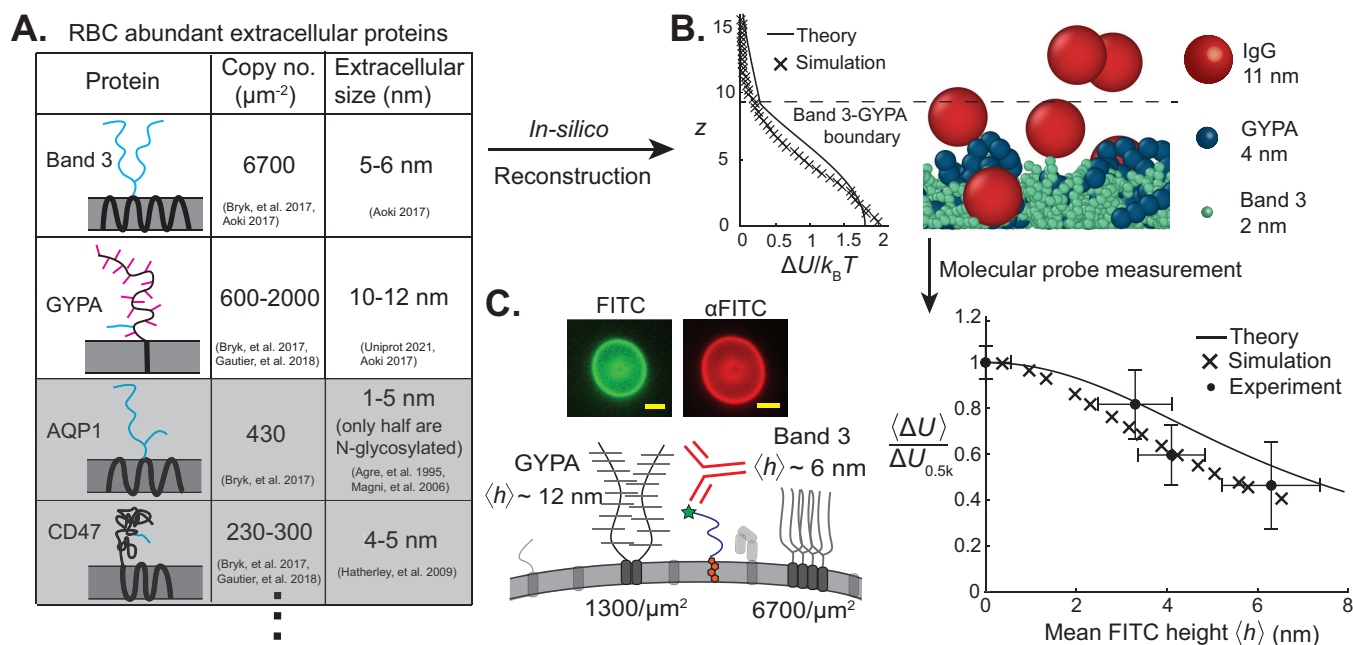


Fig. 3. Red blood cell (RBC) membrane proteomics is integrated into an in-silico model to predict surface crowding heterogeneity validated by theory and experiments. (A) Relevant data from RBC proteomics for predicting surface crowding variation with extracellular height. Four of the most abundant RBC proteins with extracellular domains (39) are characterized according to copy number and extracellular domain size (36, 39–44). Simplified schematics of transmembrane and extracellular domains are sketched in a lipid bilayer, with black peptide sequences, blue N-glycans, and magenta O-glycans. Glycophorin A (GYPA) and Band 3 are the only proteins of sufficient extracellular size and density to be considered in our model. (B) MD simulations and analytical theory describe steric repulsion between an IgG antibody and a model RBC glycocalyx. (Left) Repulsive potential ΔU from both analytical theory and MD simulation is plotted as a function of height. (Right) Snapshot of MD simulations with spherical IgG adsorbing to a bidisperse polymer brush of coarse-grained Band 3 and GYPA. (C) Molecular probes verify *in-silico* crowding heterogeneity predictions. (Upper left) Fluorescence micrographs demonstrate strong cholesterol-PEG-FITC sensor and anti-FITC IgG binding. Scale bar is 5 μm . (Lower left) Schematic of IgG binding to synthetic antigen sensors on an RBC surface, with GYPA and Band 3 dominating crowding. (Right) Mean crowding potential as a function of mean sensor height for experiments (circles). MD (crosses) and analytical theory (curve) predict decreasing mean crowding with height for each sensor.

The flexibility of the PEG linker in our synthetic antigen sensors causes the antibody to bind across a distribution of FITC heights for any given sensor. Thus, we define our experimentally-measured crowding potential for a given sensor as a mean potential $\langle \Delta U \rangle$, which can be predicted by weighting the FITC 1-D probability density P_{FITC} by the potential profile in ΔU and integrating across all space:

$$\langle \Delta U \rangle = \int_0^\infty P_{\text{FITC}}(z; \langle h \rangle) \Delta U(z) dz. \quad [2]$$

To describe P_{FITC} , we invoke the continuous Gaussian chain model of a surface-tethered polymer of mean height $\langle h \rangle$ in an ideal solvent, calculating the chain-end distribution (see Supporting Information for calculations) (34). We verified P_{FITC} with coarse-grained MD simulations of dilute surface-tethered PEG polymers, finding that the end-monomer distribution closely agrees with theory (Fig. 2B). Numerically evaluating the integral in Eq. 2 for a set of PEG-FITC sensors with mean heights $\langle h \rangle$ yields matching theoretical and computational predictions for the observed crowding profile as a function of mean sensor height (Fig. 2C).

Recasting the data from Fig. 1C in the form given by Eq. 1 and plotting as a function of the mean sensor heights reported in Fig. 1B, shows quantitative agreement with the theoretical and MD profiles developed in Eq. 2 (Fig. 2C). Our experimental and simulation data support a mechanism by which the brush sterically excludes the antibody, suggesting that our synthetic antigen sensors act as direct reporters of crowding heterogeneities with nanometer resolution.

Synthetic sensors validate crowding predictions based on red blood cell proteomics.

After validating our experimental antigen sensors on reconstituted membranes with analytical theory and coarse-grained simulations, we sought to use theoretical and computational methods synergistically with experiments to map the extracellular crowding landscape of the human red blood cell (RBC). Since the RBC surface proteome is fully-characterized (36, 39), we identified the most abundant extracellular proteins, and estimated extracellular domain sizes (Fig. 3A). In particular, we identified two abundant proteins with bulky extracellular domains (36, 39, 40): anion transporter Band 3 and mucin-like sialoglycoprotein GYPA.

Using both analytical theory and coarse-grained MD simulations, we modeled the RBC glycocalyx as a bidisperse polymer brush whose extracellular crowding profile opposes the adsorption of colloids like IgG (Fig. 3B). We used the lengths of extracellular peptides and glycans to estimate both the statistical monomer size and chain height of GYPA and Band 3 (see Supporting Information). We input predicted chain height and known chain grafting densities into a model that superimposed two parabolic polymer brush density profiles (30), and applied the scaling $\Delta U \sim \phi^{9/4}$ to model the repulsive potential (24, 35). We also developed an in-silico model of a bidisperse brush, with each protein modeled as a bead-spring polymer (see Supporting Information for coarse-graining details). Fig. 3B shows close agreement between the analytical and MD descriptions of the glycocalyx, with the MD potential decaying faster because it relaxes the assumption of

a strongly-stretched brush.

To verify our predicted z -direction crowding profile, we incubated human RBCs in our synthetic antigen sensors and observed strong membrane incorporation (Fig. 3C). We measured the dissociation constant of anti-FITC binding to PEG0.5k, 2k, 5k, and 10k sensors, normalizing by the uncrowded $K_{D,0}$ on beads to find $\langle \Delta U \rangle$ (Eq. 1). Antibody binding increased $\approx 5x$ from the most surface-proximal (PEG0.5k) to the most membrane-distal probe (PEG10k), corresponding to the crowding free energy penalty doubling from $z = 6.5\text{nm}$ to $z = 0$ (Fig. 3C). The experimental crowding landscape closely tracks the theoretical and simulated potentials, weighted by the FITC distributions in Fig. 2B.

These data demonstrate that for the relatively simple RBC plasma membrane, detailed proteomics data including copy number, structure, and glycosylation of surface proteins provide a robust approximation of membrane-orthogonal crowding heterogeneity. Computational techniques like machine learning are rapidly accelerating the identification of surface proteins and glycosylation sites (45, 46), and with more detailed characterization of glycan sequences and surface protein densities on the horizon, we expect that the in-silico reconstruction of more complex mammalian cells will become feasible. Mapping crowding heterogeneities on these nanometer length scales with simulations and molecular probes may reveal the accessibility of receptors based on height, improving our understanding of signaling and optimizing drug delivery target selection.

Development of phase-partitioning antigen sensors to measure lateral heterogeneities in surface crowding

The existence of raft-like microdomains of lipids, cholesterol, and proteins on plasma membranes has been hypothesized to govern various physiological processes, like signal transduction, endocytosis, and membrane reorganization (47–55). Levental et al. (17–19) showed that ordered raft-like domains on giant plasma membrane vesicles (GPMVs) isolated from cells are depleted of transmembrane proteins, suggesting that crowding may vary between these domains and the bulk. However, while plasma membrane vesicles form macroscopic equilibrium domains, lipids and proteins on live cells form transient 10–200 nm domains, which fluctuate on sub-second time scales (51, 56–58). As a result, the optical characterization of raft-like domains on live cells is challenging (59–61). To probe these lateral crowding heterogeneities, we used different antigen sensors that preferentially localize into ordered or disordered membrane domains to measure spatial variations in IgG binding on both reconstituted and live plasma membranes.

In this section, we present crowding measurements on phase-separated giant unilamellar vesicles (GUVs) with crowding heterogeneities, where macroscopic phase domains are easily visualized. We produced GUVs containing the ternary lipid mixture 2:2:1 1,2-dipalmitoyl-sn-glycero-3-phosphocholine (DPPC):DOPC:cholesterol that phase separates into macroscopic liquid-ordered (Lo) and liquid-disordered (Ld) domains (62). We preferentially crowded the Ld phase with 2% DOPE-PEG2k (Fig. 4A) and added DOPE-biotin and 1,2-dipalmitoyl-sn-glycero-3-phosphoethanolamine-N-(biotinyl) (DPPE-biotin) to present the biotin antigens in each phase. The biotin was located at the membrane surface, with zero height. We measured the crowding free energy penalty for α Biotin IgG binding to each domain (Fig. 4A). Consistent with the experiments in Figs. 1–2, the PEG brush inhibited antibody binding on the

crowded Ld domain and increased the normalized effective K_D by 60 % compared to the bare surface (Fig. 4B). In contrast, α biotin binding in the less crowded Lo domain did not change.

Although macroscopic phase domains on GUVs enable a simple measurement of lateral crowding heterogeneity, this approach is not possible on live cell surfaces which do not contain macroscopic phase domains. To overcome this challenge, we performed crowding measurements on SLB-coated beads with the same ternary lipid mixture, where the underlying substrate friction arrests phase domains into ≈ 90 nm nanoscopic features, similar to the size of raft-like domains (51, 63). Since the individual phase domains cannot be identified, we measured the crowding on each phase by quantifying the α biotin IgG binding on the beads containing only one type of antigen, either DPPE-biotin or DOPE-biotin.

As shown in Fig. 4B, we found that the Ld antigen (DOPE-biotin) reported a crowding penalty 7x higher than that reported by the Lo antigen (DPPE-biotin). While the absolute magnitudes of observed ΔU were higher on beads than GUVs, we attribute this difference to the lower membrane friction on GUVs enabling IgG to more easily exclude PEG2k when binding. Given the strong qualitative difference in crowding reported by antibody binding to antigens partitioning into Lo or Ld domains, we conclude that probes that preferentially associate with one phase over another are suitable reporters of lateral crowding heterogeneities in diffraction-limited domains like lipid rafts on live cells.

Antibody binding to raft-associated antigens reports lateral crowding heterogeneities on live cell surfaces

Motivated by our ability to measure crowding heterogeneities on nanoscopic phase domains on reconstituted membranes, we used laterally-segregating antigen probes to measure in-plane crowding heterogeneities on live mammalian cells. The ganglioside GM1 is known to form clusters on live cell membranes (60, 64) and to associate with raft-like domains, particularly when bound to the pentavalent cholera toxin B (CTB) (53–55). We capitalized on the raft-association of CTB by applying it to cells in culture and measuring the K_D of α CTB IgG, which is a direct reporter of crowding above raft-like domains. We compared the K_D of α CTB to that of α FITC binding to cholesterol-PEG0.5k-FITC sensors and normalized by bare values on beads, to differentiate raft-specific crowding from that of the bulk cell membrane (Fig. 4C). GM1 protrudes only 1–2 nm above the bilayer surface (64) and CTB is only about 2–3 nm in size (65), so we assume that crowding at the CTB epitope is similar to that at the bilayer surface. We observed nearly uniform partitioning of cholesterol-PEG0.5k-FITC sensors between Lo and Ld phases on GUVs (see Supporting Information), consistent with prior work showing that functionalized cholesterol tends to favor the disordered bulk due to its reduced packing efficiency (54, 66), despite native cholesterol favoring the ordered and raft-like domains (52, 62, 66, 67).

We compared raft versus bulk crowding on HeLa cells and T47D breast cancer cells, both of which have surface proteomes rich in bulky proteins (6, 68). HeLa and T47D, like many cancer cells, both express MUC1, a tall (200–500 nm), heavily glycosylated (50–90% carbohydrate by mass) mucin that can protect against destruction by the immune system (6, 69–71). MUC1 is transcribed at 10^4 copies/HeLa cell on average, about twice the average for T47D, although the distribution of MUC1 expression in T47D is broader by several orders of magnitude

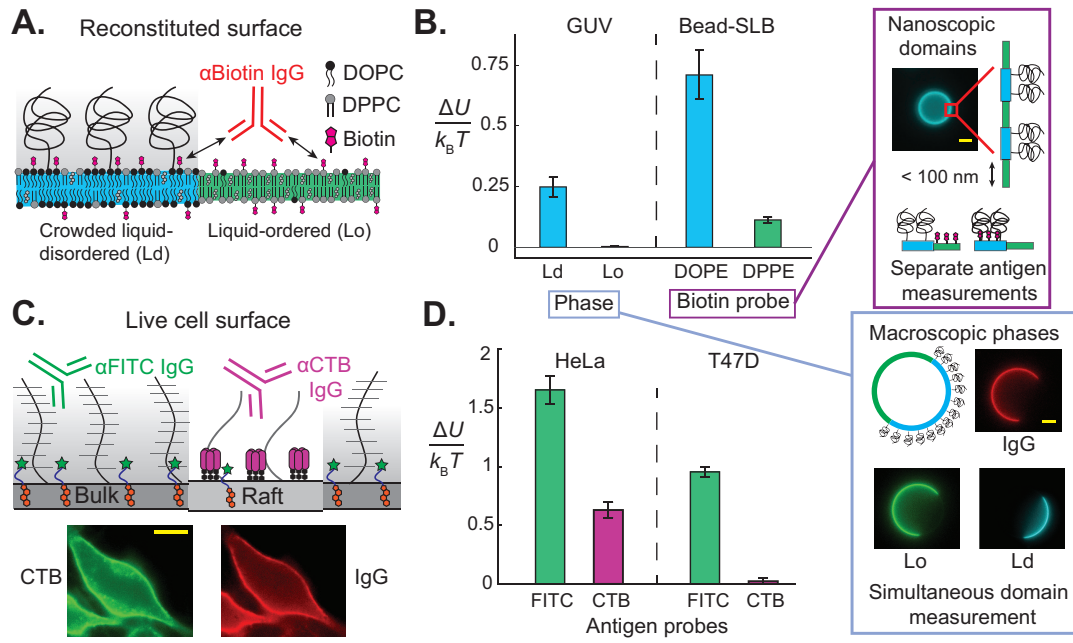


Fig. 4. Antibody binding reports lateral crowding heterogeneities on membranes with coexisting domains. (A) Reconstituted ternary lipid mixtures of DOPC/DPPC/Cholesterol containing 2% DOPE-PEG2k produce preferential surface crowding in the liquid-disordered (Ld) phase compared to the liquid-ordered (Lo) phase. DOPE- or DPPE-conjugated biotin antigens were added to enable IgG antibody binding in the two phases. (B) Direct measurement of lateral crowding heterogeneity on macroscopic phase-separated domains in giant unilamellar vesicles (GUVs) yields similar trends to indirect crowding measurement of diffraction-limited domains on lipid-coated beads. (*Left*) The crowding potential against IgG binding, due to crowding, is plotted for each domain on GUVs and for each antigen probe on kinetically-arrested SLBs on beads. (*Lower right inset*) We observed strong α biotin IgG binding (image in red) only along the bare Lo surface (green), but not along the crowded Ld surface (blue) for the phase-separated GUVs. Simultaneous imaging of IgG binding and phase domain markers enable a direct calculation of the repulsive free energy barrier differences posed by lateral crowding heterogeneities. Scale bar is 5 μ m. (*Upper right inset*) Ternary lipid mixtures on SLB-coated beads form nanoscopic domains due to arrested phase-separation caused by the underlying substrate friction, so we measured the crowding free energies with only one antigen sensor type at a time. DOPE-biotin prefers Ld and DPPE-biotin prefers Lo so their avidities serve as an analog of local crowding in their respective phases. Scale bar is 2 μ m. (C) Antigen probes partition amongst different cell membrane domains, enabling the direct characterization of lateral crowding heterogeneities on live cancer cells. (*Upper*) Cholera toxin B (CTB) antigens bind to ganglioside GM1, which associates with raft-like domains, while cholesterol-PEG0.5k-FITC slightly favors the disordered bulk membrane. α FITC or α CTB IgG binding reports lateral crowding heterogeneities between these domains. (*Lower*) HeLa cell membrane labeled with CTB-Alexa Fluor-488 and α CTB IgG-Alexa Fluor 647. Scale bar is 10 μ m. (D) Crowding free energy reported by CTB and FITC sensors on HeLa and breast cancer T47D cells.

(6, 68). Paszek et al. demonstrated a direct correlation between MUC1 expression and membrane tubule formation on both T47D and HeLa cells, suggesting MUC1 is a major contributor to surface crowding and membrane tension (6). The crowded surfaceomes of HeLa and T47D cells make these cells rich models for studying lateral heterogeneities. Bulk crowding for both cell lines as measured by our cholesterol-PEG0.5k-FITC sensors was on the order of 1-1.5 $k_B T$, consistent with the brush exclusion energy on the surface of RBCs (Fig 4D). The greater bulk crowding on HeLa cells over T47D is consistent with the greater expression of MUC1 on HeLa, although it is possible that a high density of short proteins and glycolipids is the source of the crowding differences as measured by our probes.

Surprisingly, CTB antigens reported significantly less crowding than the FITC antigen on both cells, suggesting that the extracellular space above the raft-like domains is not heavily crowded with proteins and sugars. In particular, T47D exhibited a complete elimination of its crowding free energy penalty in raft-like domains compared to the bulk membrane surface (Fig. 4D). These data are consistent with the results of Levental et al. on GPMVs (17–19), and support the hypothesis that raft-like domains of native membranes exclude proteins that contribute to extracellular crowding. This is a significant result because GPMVs exclude membrane proteins that are

bound to the actin cytoskeleton, and it was unclear whether actin, myosin, and other structural features affect the surface crowding on live cell membranes. While Mayor et al. identified the coupling between cortical actin and GPI-anchored protein clusters, our results suggest that cytoskeletal involvement does not dramatically change the concentration of bulky, disordered proteins in rafts relative to the bulk (60, 61).

Viral particles like simian virus (SV) 40 and other polyomaviruses (72, 73), and toxins like Shiga and cholera toxin (74, 75), bind to gangliosides that enrich in raft-like domains. SV40 virus is ≈ 45 nm in size (76), about three times larger than an IgG. Since the mechanical work required to insert a particle into a crowded space scales approximately as the particle volume (see Supporting Information), a viral particle would be posed with an energy barrier of $\Delta U_{\text{virus}} \sim \Delta U_{\text{IgG}} (R_{\text{virus}}/R_{\text{IgG}})^3 \approx 20 - 30 k_B T$ if it tried to penetrate the glycocalyx above the bulk membrane of T47D cells. In contrast, in the raft-like regions where the gangliosides enrich, the binding penalty is merely $\Delta U_{\text{virus}} \approx 0.5 - 1 k_B T$ on T47D cells, suggesting that viral particles may experience a thirty-fold larger effective affinity towards the less-crowded, ganglioside-rich domains.

Between the two cell lines, the ratio of bulk to raft crowding free energy is also 18x greater in T47D than in HeLa, suggesting that rafts play a cell-specific role in organizing

surface proteins. Our unique ability to probe native cell membranes will advance further mechanistic insight into the roles of the actin cytoskeleton and other structural complexities on glycocalyx organization.

Discussion

In this work, we developed a simple experimental technique to study the spatial heterogeneities of surface crowding on live cell membranes with exquisite spatial resolution. Alternative approaches like detergent resistant membranes (DRMs) and GPMVs (55) are invasive techniques that do not provide a description of surface organization in the native cell membrane environment. Prior to this work, existing techniques were capable of measuring spatial organization on cell surfaces with a very thick glycocalyx (0.2-1 μm), such as endothelial cells in the vasculature (77–80). However, studying the spatial organization of live cell surfaces with glycocalyx thicknesses of ~ 10 nm was a challenge because standard optical microscopy cannot resolve nanometer variations.

While not reporting spatial heterogeneity, recent measurements with membrane-binding macromolecular probes reported osmotic pressures of 1-4 kPa at the surface of mammalian cells (25). These surface pressures are comparable to and in some cases larger than the stiffness of the cell cortex (≈ 1 kPa), providing new insight on the physical role of protein and glycan crowding on cell membranes. In this work, we demonstrated that these pressures are highly dependent on proximity to the membrane surface and that glycocalyx crowding decays rapidly away from the membrane. Our probes are physiologically relevant because many protein-protein interactions occur at a finite distance away from the membrane, like kinetic segregation in T-cell receptor triggering (≈ 10 -15 nm) (81, 82).

We present our antigen sensors on live cell surfaces with nanometer precision and use antibody binding equilibria to directly report spatial variations in surface crowding. Our sensors achieve this nanometer spatial sensitivity by leveraging the exponential amplification of our readout (K_D) as a function of the crowding energy, $K_D \sim \exp(\Delta U/(k_B T))$ (Eq. 1). This exponential amplification distinguishes our approach from previous techniques that rely on polymer brush height as the readout of crowding, which scales weakly with surface density, $h \sim n^{1/3}$ (21, 24, 35). Taking the energy barrier to be proportional to the osmotic pressure, and in turn surface density, $\Delta U \sim \Pi \sim n^{9/4}$ (24, 35), we obtain the scaling $h \sim (\Delta U/(k_B T))^{4/27}$, which is significantly weaker than $K_D \sim \exp(\Delta U/(k_B T))$. The $\approx 1k_B T$ change in crowding we observe within 6 nm of the RBC surface confirms this spatial sensitivity, and demonstrates the power of our technique in characterizing the highly heterogeneous membrane-proximal surfaceome, in which surface signaling and viral entry occur (32, 33).

Monoclonal antibody (mAb) drug candidates are currently screened using surface-plasmon resonance (SPR), in which binding affinity and avidity are measured on a bare hydrogel chip without regard to multi-body interactions (83). With mAbs like the breast cancer treatment trastuzumab targeting a 4 nm tall epitope on human epidermal growth factor receptor 2 (HER2), probing local crowding variations may inform target selection and improve potency (33). Indeed, Chung et al. found that trastuzumab and pertuzumab attenuate tubule structures enriched in HER2, suggesting that biophysical interactions like

crowding may influence the potency of mAb therapies (84). Our crowding measurements may also help inform the biophysical mechanisms governing antibody-dependent phagocytosis, which have been recently shown to have a strong dependence on the relative heights of the macrophage Fc γ receptor and the target cell surface proteins (13, 85). In conclusion, our sensors may be used to inform important physiological processes, like antibody binding to buried surface receptors, membrane organization of lipid raft-like domains, and cellular phagocytosis.

When characterizing the RBC surface, we also demonstrated the potential to augment experimental crowding measurements with an in-silico cell surface reconstruction based upon proteomics data. As recent advances in surface proteomics continue to better characterize glycocalyx components for a broad host of cell lines (45, 46), we expect that accurate in-silico models will become possible on more complex mammalian cell surfaceomes. A technology to describe the extracellular crowding landscape for any cell a priori, using only proteomics data, may advance our basic understanding of cell membrane biology.

Using laterally-segregating antigen probes that target different plasma membrane domains, we demonstrated reduced crowding on GM1-associated raft-like domains on T47D and HeLa cells. These findings are consistent with the known reduction in transmembrane protein density on ordered domains in GPMVs (17–19), but our non-invasive measurements on live cells provide further insight into the dynamic cell surface ecosystem, including the interplay between the actin cytoskeleton and the membrane. Indeed, there has been considerable interest in the connection between the cytoskeleton and transmembrane protein organization over the past few decades (86–88), as actin is known to redistribute lipid domains on the cell surface (60, 61, 89, 90). By bridging this gap and characterizing raft-like domains on live cells, we speculate that on length scales of order 10 nm, the cytoskeleton may not dramatically change bulky protein composition beyond that of equilibrium domains, consistent with the hypothesis that GPI-anchored proteins dominate the raft proteome (17). However, the discrepancy between relative raft-to-bulk crowding on HeLa and T47D cells indicates that the role of GM1-enriched raft-like domains in organizing the glycocalyx varies considerably from cell to cell. Future direct comparisons between lateral heterogeneity on both live cells and their secreted membrane vesicles will provide a more thorough description of the fraction of extracellular bulk that remains anchored to the cytoskeleton in both disordered and raft-like membrane domains.

Materials and Methods

Antigen probe synthesis. Cholesterol-PEG $_x$ -NH $_2$, where x represents PEG0.5k, 2k, 5k, or 10k, was reacted with a 10x excess of N-hydroxy-succinimidyl ester (NHS)-FITC, overnight at 50°C in dimethylsulfoxide (DMSO). Unreacted FITC was removed via a 7K MWCO Zeba spin desalting column. SLB-coated beads were incubated with 100 nM FITC antigen sensors for 15 minutes at room temperature.

Microscope for all imaging experiments. All imaging was carried out on an inverted Nikon Ti2-Eclipse microscope (Nikon Instruments) using an oil-immersion objective (Apo 60x, numerical aperture (NA) 1.4, oil; Apo 100x, NA 1.45, oil). Lumencor SpectraX Multi-Line LED Light Source was used for excitation (Lumencor, Inc). Fluorescent light was spectrally filtered with emission filters (432/36, 515/30, 595/31, and 680/42; Semrock, IDEX Health and Science)

and imaged on a Photometrics Prime 95 CMOS Camera (Teledyne Photometrics).

Sensor height measurement. Small unilamellar vesicles (SUVs) were formed using an established sonication method (13). A lipid film containing 1,2-dioleoyl-sn-glycero-3-phosphocholine (DOPC), 3% 1,2-dioleoyl-sn-glycero-3-phosphoethanolamine-N-[methoxy(polyethylene glycol)-2000] (DOPE-PEG2k), and DOPE-rhodamine was dried under nitrogen and then vacuum for 30 minutes. The film was rehydrated in Milli-Q (MQ) water to 0.2 mg/mL lipids, sonicated at low power using a tip sonicator (Branson SFX250 Sonifier) at 20% of maximum, 1s/2s on/off, for three minutes. We added MOPS buffer at a final concentration of 50 mM MOPS pH 7.4, 100 mM NaCl to the resulting SUV mixture. Then, 10 μ L of 4 μ m silica bead slurry (10% solids) was cleaned with piranha solution (3:2 H₂SO₄:H₂O₂) and washed three times with 1 mL MQ water before being suspended in 100 μ L MQ water (1% solids). 3 μ L of bead slurry was mixed with 30 μ L SUVs and incubated for ten minutes at room temperature before washing five times with HEPES buffer (50 mM HEPES pH 7.4, 100 mM NaCl).

FITC sensor heights were established using cell surface optical profilometry (CSOP) (33). SLB-coated beads were incubated in 200 nM cholesterol-PEG_x-FITC at room temperature for 15 minutes, where *x* represents PEG0.5k, 2k, 5k, and 10k. Unbound sensors were washed from the bulk and CSOP measurement used to find the difference in apparent bead radius on the 488 nm FITC channel and 555 nm rhodamine channel ($\langle h_{\text{observed}} \rangle$). To correct for chromatic aberration, a baseline difference in 488nm and 555 nm radii ($\langle h_{\text{baseline}} \rangle$) was measured on SLB-coated beads containing DOPC with 0.05% DOPE-rhodamine, and 0.05% DOPE-Atto 488 lipids. The FITC antigen height was obtained by subtracting this baseline from the observed height: $\langle h \rangle = \langle h_{\text{observed}} \rangle - \langle h_{\text{baseline}} \rangle$.

Dissociation constant measurement for reconstituted PEG brushes.

4 μ m SLB-coated beads with PEG brushes were formed using a mixture of DOPC, 3% DSPE-PEG2k, and 0.05% DOPE-rhodamine. Bare beads for measuring $K_{D,0}$ were formed with only DOPC and 0.05% DOPE-rhodamine. Beads were incubated in 100nM cholesterol-PEG_x-FITC antigen sensors for 15 minutes at room temperature, then washed with HEPES buffer.

Lysine residues of anti-FITC (α FITC) IgG antibodies were randomly labeled by reacting with 8x excess NHS-Alexa Fluor 647 for one hour at room temperature in 50 mM sodium bicarbonate solution. Unreacted dye was separated via a 7MWCO spin desalting column and the recovery and labeling ratio measured via Nanodrop UV-vis spectroscopy.

Coverslips were passivated with 1 mM bovine serum albumin (BSA) to prevent nonspecific antibody adsorption. Antigen-coated beads were added to coverslip wells containing α FITC-647, and allowed to sediment and equilibrate with IgG for 30 minutes at room temperature. At least 50 beads were imaged for each bulk IgG concentration, with an approximately equatorial focal plane. Images were subdivided into individual beads, and the edges identified by the brightest 5% of pixels, on the 555 nm (DOPE-rhodamine) channel, for each sub-image. The background intensity was taken to be the 30th percentile of α FITC intensities for each bead subimage, and the bead intensity signal was calculated by subtracting background from the α FITC signal associated with the brightest rhodamine pixels. The intensity signal for each bead was averaged to yield a mean bead signal, and the mean bead signals were then averaged for each α FITC bulk concentration, and fit to a Hill isotherm to find K_D .

Dissociation constant measurement for CD45 antigens. A GYPA brush with dilute CD45 antigens was reconstituted by incubating beads in 10:1 GYPA:CD45. SLB-coated beads containing DOPC, 8% 1,2-dioleoyl-sn-glycero-3-[[N-(5-amino-1-carboxypentyl) iminodiacetic acid]succinyl] (DGS-Ni-NTA), and 0.2% DOPE-Atto 390 were incubated with 10 nM His-tagged mouse CD45 and 100 nM His-tagged glycophorin A (GYPA) for 15 minutes at 37°C. Unbound protein was washed five times from the bulk with HEPES buffer. GYPA was labeled with NHS-Alexa Fluor 555 and CD45 was labeled with NHS-Alexa Fluor 488, and we thus confirmed a qualitative excess of the GYPA blockers on the beads. Beads were incubated in either Alexa Fluor 647-labeled α C363 or α I3 on CD45 for 30

minutes, and the K_D measured. Baseline $K_{D,0}$ for was measured for both CD45 epitopes on beads with no GYPA.

Red blood cell (RBC) dissociation constant measurement. Single-donor human whole blood in K2-EDTA was purchased from Innovative Research and used within three days of arrival. The researchers in this study had no contact with human subjects and vendor samples were de-identified, precluding a need for IRB clearance. Blood was centrifuged at 300g for 5 minutes to isolate RBCs. RBCs were incubated with 100 nM cholesterol-PEG_x-FITC (*x* represents PEG0.5k, 2k, 5k, and 10k) antigen sensors for 15 minutes at 37°C. RBCs were added to α FITC-647, pipette mixed, and incubated for 30 minutes before imaging. RBC images were analyzed using the same methods as beads, with at least 50 cells per IgG concentration, to calculate K_D . For ΔU calculations, K_D was normalized against the bare-bead $K_{D,0}$, for each antigen.

Lateral crowding heterogeneity measurements on macroscopic membrane domains.

Antibody dissociation constants were measured on crowded and uncrowded coexisting domains in liquid-liquid phase-separated giant unilamellar vesicles (GUVs). DOPC, 1,2-dipalmitoyl-sn-glycero-3-phosphocholine (DPPC), and cholesterol were combined in a 2:2:1 ratio, which phase separates at room temperature (62). 0.3% DOPE-biotin and 0.05% 1,2-dipalmitoyl-sn-glycero-3-phosphoethanolamine-N-(biotinyl) (DPPE-biotin) were added as liquid-disordered and liquid-ordered antigen probes, respectively. We set the relative amounts of DOPE- and DPPE-biotin such that the antigen density in each phase was approximately equivalent, as reported by α Biotin binding. GUVs were formed either with or without 2% DOPE-PEG2k, which formed a crowding brush in only the liquid-disordered (Ld) phase. 0.05% each of DOPE-rhodamine and 1,2-distearoyl-sn-glycero-3-phosphoethanolamine-N-[poly(ethylene glycol)2000-N'-carboxyfluorescein] (DSPE-PEG2k-FITC) were also added to label the Ld and liquid-ordered (Lo) phases, respectively.

GUVs were produced via a modified electroformation protocol (91, 92). Lipids dissolved in chloroform were spread onto an indium tin oxide (ITO)-coated slide and the resulting film dried under vacuum for >30 minutes. The lipid film was rehydrated in a 300 mM sucrose solution, placed in contact with a second ITO-coated slide, and an AC sinusoidal voltage applied across the two slides: 10 Hz/1.0 V for two hours then 0.4V/2 Hz for 20 minutes. GUVs were electroformed at 50°C to ensure phase mixing, then cooled below the melting point to room temperature once electroformation was stopped.

Phase-separated GUVs were incubated in Alexa Fluor 647-labeled α Biotin antibody for at least 30 minutes. The GUV size distribution spanned tens of microns, requiring that each vesicle be imaged individually to preserve a consistent equatorial focus. For each vesicle, Lo and Ld domains were identified by selecting the brightest 2% of pixels on the 488 (DSPE-PEG2k-FITC) and 555 nm (DOPE-rhodamine) channels, respectively, for each GUV image. The corresponding 647 nm intensities for these pixels were averaged and subtracted from the bottom 30th percentile of 647 intensities across the entire image, yielding a mean intensity for each phase. Lo and Ld intensities were averaged across all GUVs for each bulk IgG concentration and fit to a Hill isotherm to find K_D (with DOPE-PEG2k) and $K_{D,0}$ (without DOPE-PEG2k).

Lateral crowding heterogeneity measurements on diffraction-limited domains.

Antibody dissociation constants were measured for Lo- and Ld-favoring antigens on phase-separated SLBs, with kinetically-arrested nanoscopic domains. Beads were coated with SLBs containing 2:2:1 DOPC:DPPC:cholesterol, with 0.05% DOPE-rhodamine Ld label and 1% DOPE-PEG2k Ld crowder. Only one of either DOPE-biotin or DPPE-biotin was also included, localizing the antigens primarily on either the Ld or Lo domains, respectively. Beads were incubated in α Biotin-647, imaged, and K_D fit for each antigen. $K_{D,0}$ was measured with SLBs containing no DOPE-PEG2k.

Lateral crowding heterogeneity measurements on human cancer cells.

Human cervical cancer HeLa and breast cancer T47D cells were obtained from ATCC. HeLa cells were cultured in Dulbecco's Modified Eagle Medium (DMEM) and T47D cells were cultured in RPMI 1640 Medium, both supplemented with 10% fetal bovine serum

(FBS) and and 1% Pen-Strep. Cells were incubated at 37°C with 5% CO₂.

Cells were plated approximately 24 hours before imaging. Immediately before imaging, media was exchanged with PBS containing either 100 nM cholesterol-PEG0.5k-FITC and cholesterol-PEG0.5k-Alexa Fluor 555, or 100 nM Alexa Fluor 488-labeled cholera toxin B (CTB), and incubated for 20 minutes at 37°C. Unbound antigen was washed from the well five times with PBS.

Cells were incubated in either α FITC-647 or α CTB-647 for 30 minutes. At least 15 cells were analyzed for each bulk concentration. Fluorescence images of individual cells were captured, focusing on the equatorial plane, so that the plasma membrane outline was clearly visible. To select pixels for analysis, we took the product of the antigen and antibody signal for each pixel, identifying the top 7% for analysis. We took the mean IgG signal for these pixels, for each cell, to obtain the peak signal for that cell. In HeLa and T47D cell measurements, we observed some sensor internalization into the cell interior, but the antibody largely remained on the exterior of the cell. Taking the product of IgG and antigen ensured that only plasma membrane signal was analyzed. For cells with cholesterol-PEG0.5k-FITC antigens, we used the co-incubated Alexa Fluor 555 constructs to identify the pixels of highest antigen density, because the α FITC IgG quenches FITC. The background signal was set to the bottom 30th percentile of pixels, and the mean of the differences between peak and baseline for each cell taken to represent the surface-bound antibody. Bound antibody fraction was plotted against bulk IgG concentration and fit using the Hill isotherm ($n=2$) to find K_D .

The bare dissociation constant $K_{D,0}$ for α CTB was measured on SLB-coated beads containing DOPC and 0.05% ovine brain GM1. Beads were incubated with 100 nM CTB for 15 min, washed, incubated in α CTB for one hour, and then imaged. $K_{D,0}$ was fit to IgG intensity data according to the procedures in earlier bead experiments. For the cholesterol-PEG0.5k-FITC antigen, the $K_{D,0}$ value from earlier bead experiments was used. We calculated the free energies associated with CTB-reported raft-like domain crowding and FITC-reported bulk crowding using Eq. 1.

Molecular Dynamics Simulations. To validate theoretical predictions for the surface crowding profile, we performed coarse-grained molecular dynamics simulations using a graphics processing unit (GPU)-enabled HOOMD-Blue simulation package (93, 94). We simulated membrane-bound PEG-conjugated FITC sensors using the Kremer-Grest bead-spring model (95) for polymers chains, with bead diameter $\sigma = 0.33\text{nm}$ to represent the ethylene glycol monomer. One polymer end was confined to the bottom of the simulation box using wall potentials but was allowed to diffuse laterally (33). We imposed periodic boundary conditions along x and y while the $z = \pm L_z/2$ boundaries were impenetrable. We used a system box size of $V = L^2 L_z$ where $L_z = 50 - 200\sigma$ and L was adjusted to achieve the specified surface density and number of chains. All particle pair interactions and wall potentials are modeled using the Weeks-Chandler-Anderson potential (96). The bond potentials were modeled using the finite extensible nonlinear elastic (FENE) potential with spring constant $k = k_B T / \sigma^2$. The semiflexibility of polymer chains was imposed through a harmonic angle potential $U_B = \epsilon_B (1 - \cos(\theta_{ijk} - \theta_0))$, where θ_{ijk} is the bond angle between adjacent particles (i, j, k), θ_0 is the resting angle, and $\epsilon_B = k_B T L_P / L_B$ is the bending energy, defined with persistence length $L_P = 0.97\sigma$ and bond length $L_B = \sigma$. We first simulated the experimental surface density of ~ 1000 chains/ μm^2 and averaged over ~ 2000 polymers to verify that chains were dilute and non-interacting. We then simulated single chains and varied the degrees of polymerization to span PEG0.5k to PEG10k. Using simulation snapshots, we binned the spatial distribution of the FITC sensor normal to the surface, P_{FITC} . Single-chain dynamics were averaged over 15 simulations of 1000 snapshots each.

To characterize surface crowding, we separately simulated spherical antibody particles in the presence of surface-confined polymers. PEG2k crowders on reconstituted beads were modeled as a monodisperse polymer brush with degree of polymerization $N = 45$ and surface density of $30000/\mu\text{m}^2$ and averaged over ~ 1000 chains. In separate simulations, we also modeled RBC cell surface proteins using a bidisperse polymer brush with the same coarse-graining as PEG. GYPA was coarse-grained into a 7-bead chain with a bead

diameter of 4 nm, corresponding to the size of the sugar side chains along the backbone. Band 3 was coarse-grained into a 10-bead chain with 2 nm beads, representing the two large branches of the N-glycan. We chose surface coverages of 1300 and 6700 chains/ μm^2 to match reported copy numbers of GYPA and Band 3. The Fab region of IgG was coarse-grained into a single spherical bead of size 4 nm in simulations of the reconstituted PEG2k brush, while the full IgG antibody was coarse-grained into an 11 nm bead in simulations of the RBC surface. The 2-3 nm PEG2k brush is smaller than a ~ 10 nm IgG, so we assume only the Fab domain penetrates the reconstituted brush, while the full IgG penetrates the thicker RBC glycocalyx (97, 98).

We calculated the probability distribution of antibodies on the cell surface in the presence of crowding polymers or proteins, and used the Boltzmann relation to compute the brush repulsive potential $U_{\text{brush}}(z) = -\ln(P_{\text{IgG}}(z)/P_{\text{bulk}})$ at equilibrium. We numerically integrated Eq. 2 to compute the mean crowding potential $\langle \Delta U \rangle$ given height fluctuations in the FITC sensor (Figs. 2C, 3B).

ACKNOWLEDGMENTS. This material is based upon work supported by the National Science Foundation under Grant No. 2150686. D.P.A. is supported by the National Science Foundation Graduate Research Fellowship under Grant No. 2139319. Y.X. is supported by the Dow Chemical Discovery Fellowship in the Department of Chemical Engineering at the University of California, Santa Barbara. S.C.T. is supported by the Packard Fellowship in Science and Engineering. The authors acknowledge the assistance of Dr. Jennifer Smith, manager of the Biological Nanostructures Laboratory within the California NanoSystems Institute, supported by the University of California, Santa Barbara. Use was made of computational facilities purchased with funds from the National Science Foundation (CNS-1725797) and administered by the Center for Scientific Computing (CSC). The CSC is supported by the California NanoSystems Institute and the Materials Research Science and Engineering Center (MRSEC; NSF DMR 1720256) at UC Santa Barbara.

1. WT Snead, et al., Membrane fission by protein crowding. *Proc. Natl. Acad. Sci. United States Am.* **114**, E3258–E3267 (2017).
2. JC Stachowiak, et al., Membrane bending by protein-protein crowding. *Nat. Cell Biol.* **14**, 944–949 (2012).
3. DJ Busch, et al., Intrinsically disordered proteins drive membrane curvature. *Nat. Commun.* **6** (2015).
4. Z Chen, E Atefi, T Baumgart, Membrane shape instability induced by protein crowding. *Biophys. J.* **111**, 1823–1826 (2016).
5. WF Zeno, KE Johnson, DY Sasaki, SH Risbud, ML Longo, Dynamics of crowding-induced mixing in phase separated lipid bilayers. *J. Phys. Chem. B* **120**, 11180–11190 (2016).
6. CR Shurer, et al., Physical principles of membrane shape regulation by the glycocalyx. *Cell* **177**, 1757–1770.e21 (2019).
7. WT Snead, et al., Bar scaffolds drive membrane fission by crowding disordered domains. *J. Cell Biol.* **218**, 664–682 (2019).
8. DJ Honigfort, MO Altman, P Gagneux, K Godula, Glycocalyx crowding with mucin mimetics strengthens binding of soluble and virus-associated lectins to host cell glycan receptors. *Proc. Natl. Acad. Sci.* **118**, e2107896118 (2021).
9. S Rex, MJ Zuckermann, M Laffeur, JR Silvius, Experimental and monte carlo simulation studies of the thermodynamics of polyethyleneglycol chains grafted to lipid bilayers. *Biophys. J.* **75**, 2900–2914 (1998).
10. H Du, P Chandaroy, SW Hui, Grafted poly-(ethylene glycol) on lipid surfaces inhibits protein adsorption and cell adhesion. *Biochimica et Biophys. Acta (BBA) - Biomembr.* **1326**, 236–248 (1997).
11. R Leventis, JR Silvius, Quantitative experimental assessment of macromolecular crowding effects at membrane surfaces. *Biophys. J.* **99**, 2125–2133 (2010).
12. H Jung, et al., Impact of hapten presentation on antibody binding at lipid membrane interfaces. *Biophys. J.* **94**, 3094–3103 (2008).
13. MH Bakalar, et al., Size-dependent segregation controls macrophage phagocytosis of antibody-opsonized targets. *Cell* **174**, 131–142.e13 (2018) HeLa surface area 1600um.
14. N Güll, MV Egmond, Antibody-dependent phagocytosis of tumor cells by macrophages: A potent effector mechanism of monoclonal antibody therapy of cancer. *Cancer Res.* **75**, 5008–5013 (2015).
15. JCH Kuo, MJ Paszek, Glycocalyx curving the membrane: Forces emerging from the cell exterior. *Annu. Rev. Cell Dev. Biol.* **37**, 257–283 (2021).
16. M Löwe, M Kalacheva, AJ Boersma, A Kedrov, The more the merrier: effects of macromolecular crowding on the structure and dynamics of biological membranes. *FEBS J.* **287**, 5039–5067 (2020).
17. I Levental, M Grzybek, K Simons, Raft domains of variable properties and compositions in plasma membrane vesicles. *Proc. Natl. Acad. Sci. United States Am.* **108**, 11411–11416 (2011).

18. KR Levental, I Levental, Chapter two - giant plasma membrane vesicles: Models for understanding membrane organization (2015).
19. I Levental, KR Levental, FA Heberle, Lipid rafts: Controversies resolved, mysteries remain. *Trends Cell Biol.* **30**, 341–353 (2020).
20. JM Noble, et al., Direct comparison of optical and electron microscopy methods for structural characterization of extracellular vesicles. *J. Struct. Biol.* **210** (2020).
21. JR Houser, CC Hayden, D Thirumalai, JC Stachowiak, A Förster resonance energy transfer-based sensor of steric pressure on membrane surfaces. *J. Am. Chem. Soc.* **142**, 20796–20805 (2020).
22. PG de Gennes, Polymers at an interface; a simplified view. *Adv. Colloid Interface Sci.* **27**, 189–209 (1987).
23. ST Milner, Polymer brushes. *Science* **251**, 905–914 (1991).
24. M Rubinstein, R Colby, *Polymer Physics*. (Oxford University Press), 1 edition, (2003).
25. SC Takatori, S Son, D Lee, DA Fletcher, Engineered molecular sensors of cell surface crowding. *bioRxiv* (2022).
26. D Bausch-Fluck, et al., The in silico human surfaceome. *Proc. Natl. Acad. Sci. United States Am.* **115**, E10988–E10997 (2018).
27. C Klijn, et al., A comprehensive transcriptional portrait of human cancer cell lines. *Nat. Biotechnol.* **33**, 306–312 (2015).
28. SB Pollock, et al., Highly multiplexed and quantitative cell-surface protein profiling using genetically barcoded antibodies. *Proc. Natl. Acad. Sci. United States Am.* **115**, 2836–2841 (2018).
29. M Stoekius, et al., Simultaneous epitope and transcriptome measurement in single cells. *Nat. Methods* **14**, 865–868 (2017).
30. ST Milner, TA Witten, ME Cates, Theory of the grafted polymer brush. *Macromolecules* **21**, 2610–2619 (1988).
31. AM Tom, WK Kim, C Hyeon, Polymer brush-induced depletion interactions and clustering of membrane proteins. *The J. Chem. Phys.* **154**, 214901 (2021).
32. CS Delaveris, ER Webster, SM Banik, SG Boxer, CR Bertozzi, Membrane-tethered mucin-like polypeptides sterically inhibit binding and slow fusion kinetics of influenza A virus. *Proc. Natl. Acad. Sci. United States Am.* **117**, 12643–12650 (2020).
33. S Son, et al., Molecular height measurement by cell surface optical profilometry (csop). *Proc. Natl. Acad. Sci. United States Am.* **117**, 14209–14219 (2020).
34. WB Russel, DA Saville, WR Schowalter, *Colloidal Dispersions*. (Cambridge University Press), (1989).
35. A Halperin, Polymer brushes that resist adsorption of model proteins: Design parameters. *Langmuir* **15**, 2525–2533 (1999).
36. T Aoki, A comprehensive review of our current understanding of red blood cell (rbc) glycoproteins. *Membranes* **7**, 1–19 (2017).
37. J Paturej, SS Sheiko, S Panyukov, M Rubinstein, Molecular structure of bottlebrush polymers in melts. *Sci. Adv.* **2** (2016).
38. AK Kenworthy, K Hristova, D Needham, TJ McIntosh, Range and magnitude of the steric pressure between bilayers containing phospholipids with covalently attached poly(ethylene glycol). *Biophys. J.* **68**, 1921–1936 (1995).
39. AH Bryk, JR Wiśniewski, Quantitative analysis of human red blood cell proteome. *J. Proteome Res.* **16**, 2752–2761 (2017).
40. EF Gautier, et al., Absolute proteome quantification of highly purified populations of circulating reticulocytes and mature erythrocytes. *Blood Adv.* **2**, 2646–2657 (2018).
41. P Agre, BL Smith, GM Preston, Abh and colton blood group antigens on aquaporin-1, the human red cell water channel protein. *Transfus. Clinique* **2**, 303–308 (1995).
42. A Bateman, et al., Uniprot: the universal protein knowledgebase in 2021. *Nucleic Acids Res.* **49**, D480–D489 (2021).
43. F Magni, et al., Proteomic knowledge of human aquaporins. *PROTEOMICS* **6**, 5637–5649 (2006).
44. D Hatherley, SC Graham, K Harlos, DI Stuart, A Barclay, Structure of signal-regulatory protein α . *J. Biol. Chem.* **284**, 26613–26619 (2009).
45. D Bausch-Fluck, et al., A mass spectrometric-derived cell surface protein atlas. *PLoS ONE* **10**, 1–22 (2015).
46. Z Zhou, C Ye, J Wang, NR Zhang, Surface protein imputation from single cell transcriptomes by deep neural networks. *Nat. Commun.* **11**, 1–10 (2020).
47. K Simons, JL Sampaio, Membrane organization and lipid rafts. *Cold Spring Harb. Perspectives Biol.* **3**, 1–17 (2011).
48. M Carquin, L D'Auria, H Pollet, ER Bongarzone, D Tyteca, Recent progress on lipid lateral heterogeneity in plasma membranes: From rafts to submicrometric domains. *Prog. Lipid Res.* **62**, 1–24 (2016).
49. DA Brown, E London, Functions of lipid rafts in biological membranes. *Annu. Rev. Cell Dev. Biol.* **14**, 111–136 (1998).
50. K Simons, E Ikonen, Functional rafts in cell membranes. *Nature* **387**, 569–572 (1997).
51. D Lingwood, K Simons, Lipid rafts as a membrane-organizing principle. *Science* **327**, 46–50 (2010).
52. DA Brown, E London, Structure and function of sphingolipid- and cholesterol-rich membrane rafts. *J. Biol. Chem.* **275**, 17221–17224 (2000).
53. JR Silvius, Partitioning of membrane molecules between raft and non-raft domains: Insights from model-membrane studies. *Biochimica et Biophys. Acta - Mol. Cell Res.* **1746**, 193–202 (2005).
54. AS Klymchenko, R Kreder, Fluorescent probes for lipid rafts: From model membranes to living cells. *Chem. Biol.* **21**, 97–113 (2014).
55. JH Lorent, I Levental, Structural determinants of protein partitioning into ordered membrane domains and lipid rafts. *Chem. Phys. Lipids* **192**, 23–32 (2015).
56. E Sezgin, et al., Elucidating membrane structure and protein behavior using giant plasma membrane vesicles. *Nat. Protoc.* **7**, 1042–1051 (2012).
57. LJ Pike, Lipid rafts: Bringing order to chaos. *J. Lipid Res.* **44**, 655–667 (2003).
58. K Jacobson, P Liu, BC Lagerholm, The lateral organization and mobility of plasma membrane components. *Cell* **177**, 806–819 (2019).
59. BF Lillemeier, JR Pfeiffer, Z Surviladze, BS Wilson, MM Davis, Plasma membrane-associated proteins are clustered into islands attached to the cytoskeleton. *Proc. Natl. Acad. Sci. United States Am.* **103**, 18992–18997 (2006).
60. T Skotland, K Sandvig, The role of ps 18:0/18:1 in membrane function. *Nat. Commun.* **10**, 1–10 (2019).
61. R Raghupathy, et al., Transbilayer lipid interactions mediate nanoclustering of lipid-anchored proteins. *Cell* **161**, 581–594 (2015).
62. SL Veatch, SL Keller, Separation of liquid phases in giant vesicles of ternary mixtures of phospholipids and cholesterol. *Biophys. J.* **85**, 3074–3083 (2003).
63. A Honigsmann, V Mueller, SW Hell, C Eggeling, Sted microscopy detects and quantifies liquid phase separation in lipid membranes using a new far-red emitting fluorescent phosphoglycerolipid analogue. *Faraday Discuss.* **161**, 77–89 (2012).
64. J Shi, et al., Gm1 clustering inhibits cholera toxin binding in supported phospholipid membranes. *J. Am. Chem. Soc.* **129**, 5954–5961 (2007).
65. N Ohtomo, T Muraoka, A Tashiro, Y Zinnaka, K Amako, Size and structure of the cholera toxin molecule and its subunits. *The J. Infectious Diseases* **133** Suppl., 31–40 (1976).
66. T Baumgart, G Hunt, ER Farkas, WW Webb, GW Feigenson, Fluorescence probe partitioning between lo/ld phases in lipid membranes. *Biochimica et Biophys. Acta - Biomembr.* **1768**, 2182–2194 (2007).
67. AG Ostermeyer, BT Beckrich, KA Ivarson, KE Grove, DA Brown, Glycosphingolipids are not essential for formation of detergent-resistant membrane rafts in melanoma cells. methyl- β -cyclodextrin does not affect cell surface transport of a gpi-anchored protein. *J. Biol. Chem.* **274**, 34459–34466 (1999).
68. N Nagaraj, et al., Deep proteome and transcriptome mapping of a human cancer cell line. *Mol. Syst. Biol.* **7**, 1–8 (2011).
69. CL Hattrup, SJ Gendler, Structure and function of the cell surface (tethered) mucins. *Annu. Rev. Physiol.* **70**, 431–457 (2008).
70. M Brayman, A Thathiah, DD Carson, Muc1: A multifunctional cell surface component of reproductive tissue epithelia. *Reproductive Biol. Endocrinol.* **2**, 1–9 (2004).
71. K Zhang, R Sikut, GC Hansson, A muc1 mucin secreted from a colon carcinoma cell line inhibits target cell lysis by natural killer cells. *Cell. Immunol.* **176**, 158–165 (1997).
72. M Qian, D Cai, KJ Verhey, B Tsai, A lipid receptor sorts polyomavirus from the endolysosome to the endoplasmic reticulum to cause infection. *PLoS Pathog.* **5** (2009).
73. S Engel, et al., Role of endosomes in simian virus 40 entry and infection. *J. Virol.* **85**, 4198–4211 (2011).
74. K Sandvig, J Bergan, AB Dyve, T Skotland, ML Torgersen, Endocytosis and retrograde transport of shiga toxin. *Toxicol.* **56**, 1181–1185 (2010).
75. Y Fujinaga, et al., Gangliosides that associate with lipid rafts mediate transport of cholera and related toxins from the plasma membrane to endoplasmic reticulum. *Mol. Biol. Cell* **14**, 4783–4793 (2003).
76. MG Rosmalen, et al., Revealing in real-time a multistep assembly mechanism for sv40 virus-like particles. *Sci. Adv.* **6**, 1–8 (2020).
77. S Weinbaum, JM Tarbell, ER Damiano, The structure and function of the endothelial glycocalyx layer. *Annu. Rev. Biomed. Eng.* **9**, 121–167 (2007).
78. JM Tarbell, LM Cancel, The glycocalyx and its significance in human medicine. *J. Intern. Medicine* **280**, 97–113 (2016).
79. S Weinbaum, LM Cancel, BM Fu, JM Tarbell, The glycocalyx and its role in vascular physiology and vascular related diseases. *Cardiovasc. Eng. Technol.* **12**, 37–71 (2021).
80. CC Michel, Starling: The formulation of his hypothesis of microvascular fluid exchange and its significance after 100 years. *Exp. Physiol.* **82**, 1–30 (1997).
81. SJ Davis, PA van der Merwe, The kinetic-segregation model: TCR triggering and beyond. *Nat. Immunol.* **7**, 803–809 (2006).
82. AS Shaw, ML Dustin, Making the T cell receptor go the distance: A topological view of T cell activation. *Immunity* **6**, 361–369 (1997).
83. D Lakayan, R Haselberg, R Gahoual, GW Somsen, J Kool, Affinity profiling of monoclonal antibody and antibody-drug-conjugate preparations by coupled liquid chromatography-surface plasmon resonance biosensing. *Anal. Bioanal. Chem.* **410**, 7837–7848 (2018).
84. I Chung, et al., High cell-surface density of her2 deforms cell membranes. *Nat. Commun.* **7** (2016).
85. EC Suter, et al., Antibody:cd47 ratio regulates macrophage phagocytosis through competitive receptor phosphorylation. *Cell Reports* **36**, 109587 (2021).
86. A Kusumi, et al., Dynamic organizing principles of the plasma membrane that regulate signal transduction: Commemorating the fortieth anniversary of singer and nicolson's fluid-mosaic model. *Annu. Rev. Cell Dev. Biol.* **28**, 215–250 (2012).
87. A Kusumi, Y Sako, Cell surface organization by the membrane skeleton. *Curr. Opin. Cell Biol.* **8**, 566–574 (1996).
88. K Ritchie, R Iino, T Fujiwara, K Murase, A Kusumi, The fence and picket structure of the plasma membrane of live cells as revealed by single molecule techniques (review). *Mol. Membr. Biol.* **20**, 13–18 (2003).
89. A Honigsmann, et al., A lipid bound actin meshwork organizes liquid phase separation in model membranes. *eLife* **2014**, 1–16 (2014).
90. C Gómez-Moutón, et al., Segregation of leading-edge and uropod components into specific lipid rafts during T cell polarization. *Proc. Natl. Acad. Sci.* **98**, 9642–9647 (2001).
91. MI Angelova, DS Dimitrov, Liposome electroformation. *Faraday Discuss. Chem. Soc.* **81**, 303 (1986).
92. EM Schmid, DL Richmond, DA Fletcher, Reconstitution of proteins on electroformed giant unilamellar vesicles (2015).
93. JA Anderson, et al., General purpose molecular dynamics simulations fully implemented on graphics processing units. *JCoPh* **227**, 5342–5359 (2008).
94. JA Anderson, J Glaser, SC Glotzer, HOOMD-blue: A Python package for high-performance molecular dynamics and hard particle Monte Carlo simulations. *Comput. Mater. Sci.* **173** (2020).
95. K Kremer, GS Grest, Dynamics of entangled linear polymer melts: A molecular-dynamics simulation. *The J. Chem. Phys.* **92**, 5057–5086 (1990).

96. JD Weeks, D Chandler, HC Andersen, Role of Repulsive Forces in Determining the Equilibrium Structure of Simple Liquids. *The J. Chem. Phys.* **54**, 5237 (1971).
97. CD Michele, PDL Rios, G Foffi, F Piazza, Simulation and theory of antibody binding to crowded antigen-covered surfaces. *PLoS Comput. Biol.* **12**, 1–17 (2016).
98. YH Tan, et al., A nanoengineering approach for investigation and regulation of protein immobilization. *ACS Nano* **2**, 2374–2384 (2008).

Supplementary Appendix for
Antibody binding reports spatial heterogeneities in cell membrane organization

Daniel P. Arnold, Yaxin Xu, and Sho C. Takatori

This document contains:

Supplementary Text
Figures S1-S7
Legends for Movies S1-S3
SI References

Other supplementary materials for this manuscript include the following:

Movies S1-S3

Supplementary Text

Theory Development

Antibody insertion into a semidilute polymer suspension

To describe the crowding-mediated free energy barrier to antibody binding, we invoke the theory of a hard colloid in a nonadsorbing polymer suspension by Louis et al. [1]. We assume that the free energy penalty of inserting the colloidal antibody into the brush is dominated by entropic effects arising from the exclusion of monomer density from the volume occupied by the colloid V , as well as the creation of an interface of area A_s around the colloid. Thus, the free energy can be defined in terms of the osmotic pressure Π and interfacial tension γ .

$$\Delta U = \Pi(\phi) V + \gamma(\phi) A_s \quad (1)$$

Brush osmotic pressure

The osmotic pressure can be defined in terms of the monomer volume fraction ϕ via the virial equation of state [2]

$$\Pi(\phi) = \frac{k_B T}{\nu_p N} \phi (1 + A_2 \phi + A_3 \phi^2 + \dots) \quad (2)$$

where ν_p is the volume of a monomer, N is degree of polymerization, and A_2 and A_3 are the dimensionless second and third virial coefficients. We operate in the semi-dilute limit with high interpenetration between chains, such that $\phi/\phi^* \gg 1$, where ϕ^* is the chain overlap volume fraction. Thus the osmotic pressure can be expressed as

$$\Pi = \frac{k_B T}{\nu_p N} \phi \left(1 + C_2 \frac{\phi}{\phi^*} + \dots \right) \sim \frac{k_B T}{\nu_p N} \phi \left(\frac{\phi}{\phi^*} \right)^m. \quad (3)$$

Upon substituting the scaling $\phi^* \sim N^{-4/5}$, we can express osmotic pressure as

$$\Pi \sim \frac{k_B T}{\nu_p N} \phi^{m+1} N^{4m/5-1}. \quad (4)$$

Upon assuming that the dominant multi-body interactions between monomers are independent of chain identity, we can impose the constraint that the osmotic pressure must be independent of degree of polymerization. Thus $m = 5/4$ and we achieve the scaling

$$\Pi \sim \phi^{9/4}, \quad (5)$$

which is well-known in the polymer literature [2, 3].

Surface tension

In the continuum limit, the antibody diameter is much larger than the monomers such that curvature can be neglected when calculating interfacial tension. Thus we may apply the following relation for interfacial tension near a wall [1]

$$\gamma(\phi) = -\Pi(\phi) \Gamma(\phi) + \int_0^\phi \Pi(\phi') \frac{\partial \Gamma(\phi')}{\partial \phi'} d\phi' \quad (6)$$

where Γ is the reduced adsorption, defined by the depletion of nonadsorbing hard sphere monomers as a function of distance r from the colloid surface:

$$\Gamma = \int_0^\infty \left(\frac{\phi(r)}{\phi(r \rightarrow \infty)} - 1 \right) dr. \quad (7)$$

If the monomer density is sufficiently small such that polymer-colloid interactions far outweigh polymer-polymer interactions, then Γ will be independent of ϕ and the first term of Eq. 6 will dominate. Further assuming an ideal brush gives $\Gamma \approx -2R_g/\sqrt{\pi} \approx R_g$ and reduces Eq. 6 to $\gamma = \Pi(\phi) R_g$. Thus we approximate the interfacial free energy to be the virtual work of creating a cavity of volume $R_g A_s$ around the colloid. Thus we define an effective volume $V^{\text{eff}} = \frac{4}{3}\pi R^3 + 4\pi R^2 R_g$ such that the free energy of including a colloidal antibody into a polymer brush depends solely on the osmotic pressure:

$$\Delta U \approx \Pi(\phi) V^{\text{eff}}. \quad (8)$$

Crowding landscape of a polymer brush

We invoke the Milner, Witten, and Cates [4] self-consistent field (SCF) description of the monomer distribution in a semidilute polymer brush, to predict glycocalyx crowding variation with height. In the limit of strong stretching, the monomer volume fraction approximately follows a parabolic form as a function of height z above the grafting surface

$$\phi(z) = \phi_s \left[1 - \left(\frac{z}{L_0} \right)^2 \right]. \quad (9)$$

Here ϕ_s is the surface volume fraction $\phi(z=0)$ and L_0 is the height at which monomer density reaches approximately zero. For a PEG2k brush, we measured $\langle h \rangle$ and thus set the brush size using the relation $L_0 = 16\langle h \rangle/3\pi$. Substituting the osmotic pressure scaling in Eq. 8 and assuming the exclusion of antibody to scale linearly with osmotic pressure as in Eq. 5, yields a theoretical crowding potential profile

$$\frac{\Delta U}{k_B T} = \Delta U_{0.5k} \left[1 - \left(\frac{z}{L_0} \right)^2 \right]^{9/4}. \quad (10)$$

where $\Delta U_{0.5k} = \Delta U(z=0)$ is the potential at the brush surface, reported by the PEG0.5k sensors in our experiments.

Accounting for antigen flexibility

In Fig. S1A, ΔU represents the repulsive potential experienced by a colloid, like an antibody, inserted into a brush at a single height z . However, in our synthetic antigen sensors, the PEG chains linking the FITC antigens to the cholesterol anchors are flexible, enabling FITC to sample a distribution of heights $P_{\text{FITC}}(z)$ with mean height $\langle h \rangle$. In our experiments, for a sensor of a given PEG molecular weight, we measure $\langle h \rangle$ using CSOP and a mean potential $\langle \Delta U \rangle$ that encodes crowding data across the domain of P_{FITC} . Therefore, we weighted the potential distribution predicted by Eq. 10 by P_{FITC} to predict $\langle \Delta U \rangle$ for PEG sensors of a given $\langle h \rangle$.

$$\langle \Delta U \rangle = \int_0^\infty \Delta U(z) P_{\text{FITC}}(z) dz \quad (11)$$

Simulation results showed that the antigen PEG chains behave largely as polymer mushrooms rather than brushes, so we predicted P_{FITC} using an SCF model for a continuous Gaussian chain [5]. In the case of an ideal, dilute chain with N monomers of length l , and with one endpoint tethered at $z=0$, the density of configurations G for a chain with end-monomer position z is

$$G(z) = \left(\frac{3}{2\pi l^2 N} \right)^{1/2} \left[\exp\left(\frac{-3(z-l/2)^2}{2l^2 N} \right) - \exp\left(\frac{-3(z+l/2)^2}{2l^2 N} \right) \right]. \quad (12)$$

Thus, the normalized FITC probability distribution for a chain of given l and N is

$$P_{\text{FITC}} = \frac{G(z)}{\int_0^\infty G(z) dz} = \frac{\exp\left(\frac{-3(z-l/2)^2}{2l^2N}\right) - \exp\left(\frac{-3(z+l/2)^2}{2l^2N}\right)}{l\sqrt{\frac{2\pi N}{3}} \operatorname{erf}\left(\sqrt{\frac{3}{8N}}\right)}, \quad (13)$$

which is plotted in Fig S1B for PEG ($l = 0.6\text{nm}$) [5]. We numerically integrated Eq. 11 across all space for a series of sensors with varying N , and therefore $\langle h \rangle$, amongst a PEG2k blocking brush with the potential profile described by Eq. 10. The result is a single weighted potential value that depends on mean sensor height $\langle \Delta U \rangle$ ($\langle h \rangle$), plotted in Fig. S1C as well as main text Fig. 2B.

Red blood cell bidisperse polymer brush

In our theoretical description of red blood cells (RBC), we modified the Milner, Witten, and Cates SCF brush to account for the contributions of two crowding proteins: Glycophorin A (GYPA) and Band 3.

Glycophorin A has 72 disordered extracellular residues with 15 four-sugar O-glycans and one eight-sugar N-glycan [6]. We assume each sugar to be approximately 1 nm in size, and thus approximate the statistical segment length to be of similar size to the side chains, $l = 4$ nm. With 72 amino acids, we approximate the contour length to be $L = 26$ nm, giving $N = 6.5$ statistical segments. For a self-avoiding chain, the corresponding root-mean-squared end-to-end distance $\langle R^2 \rangle^{1/2} = N^{0.588}l = 12$ nm [2]. We thus approximate GYPA to have a mean height $\langle h \rangle = 12$ nm, so that $L_0 \approx 20$ nm. Band 3 has a two-pronged N-linked glycan with the longer fork being 19 sugars long, such that $L \approx 19$ nm [6]. We assume the two forks to be of a similar size and consider each glycan to contain two chains of size $N = 19$ with $l = 1$ nm, with a mean height of $\langle h \rangle = 5.6$ nm.

Based on proteomics data, we approximate a GYPA grafting density of $1300/\mu\text{m}^2$ and a Band 3 density of $6700/\mu\text{m}^2$ [6–8]. We estimate the surface volume fraction ϕ_s prefactor in Eq. 9 to be

$$\phi_s \approx \left(\frac{l^2}{n}\right)^{2/3} \quad (14)$$

where n is the chain grafting density on the surface [3]. Thus, we approximate $\phi_{s,\text{Band3}} \approx 0.070$ and $\phi_{s,\text{GYPA}} \approx 0.075$. Finally, we superimposed the volume fraction profiles given by Eq. 9 for each polymer, to approximate the total volume fraction distribution above the surface to be

$$\phi = \phi_{\text{band3}} + \phi_{\text{GYPA}}, \quad (15)$$

shown in Fig. S2B. By applying the scaling in Eq. 5, we obtain the bidisperse brush potential ΔU plotted in Fig. S2C.

We account for the flexibility of PEG-FITC sensors by weighting the bidisperse ΔU by the FITC distribution in Eq. 13 for a series of sensors with mean height $\langle h \rangle$, and then integrating Eq. 11. The weighted brush potential is plotted as a function of FITC mean height in Fig. S2D.

The Hill isotherm provides a superior fit for binding data

To determine the dissociation constant K_D , fluorescence intensities I of bound antibody on the bead surface were normalized to a saturation intensity I_∞ , and the resulting fraction of bound species $\theta = I/I_\infty$ fit to a binding isotherm as a function of bulk concentration c_{bulk} . The commonly-used Langmuir isotherm, which assumes monovalent binding and no interaction between bound species, is of the form

$$\theta = \frac{c_{\text{bulk}}}{K_D + c_{\text{bulk}}}. \quad (16)$$

Fig. S3A offers an example of our IgG binding data, which follows a form similar to the Langmuir isotherm at large bulk concentrations, but deviates from the approximately linear, concave-down behavior at low c_{bulk} . We consistently observed this deviation across all of our samples, suggesting polyvalency, cooperative interactions between bound species, or other nonideal effects may warrant the use of a different isotherm.

Polyvalent proteins do not always follow the Langmuir model when binding to ligands on a fluid lipid bilayer, as individual binding events may not occur independently of one another [9]. Cremer et al. demonstrated this effect with cholera toxin B (CTB), a pentavalent protein that binds to ganglioside GM1 [9]. Cremer et al. fit CTB binding data to the Hill isotherm (Eq. 17), which includes a cooperativity exponent n and recovers the Langmuir isotherm in the $n = 1$, finding that n increased with ligand density, ultimately saturating at $n = 2$ [9].

$$\theta = \frac{c_{\text{bulk}}^n}{K_{\text{D}}^n + c_{\text{bulk}}^n} \quad (17)$$

Similar experiments on IgG have also demonstrated a cooperative relationship between the first and second binding events of the two Fab arms, when binding to small molecule haptens on supported lipid bilayers [10, 11]. Cremer et al. [10, 12] further proposed a modified form of the Langmuir isotherm

$$\theta = \frac{\alpha c_{\text{bulk}}}{K_{\text{D}} + c_{\text{bulk}}}. \quad (18)$$

Here α varies with the number of available sites on the surface, defined by the difference between the total concentration of haptens on the surface and the concentration of bound haptens: $c_{\text{s}} = c_{\text{s,total}} - c_{\text{s,bound}}$, and follows the form

$$\alpha = \frac{K_{\text{D},2} + c_{\text{s}}}{K_{\text{D},2} + 2c_{\text{s}}}. \quad (19)$$

In this model, the number of available sites decreases with c_{bulk} , causing α to increase with c_{bulk} , implying positive cooperativity of IgG.

In light of the evidence of polyvalent proteins like IgG binding cooperatively on lipid bilayers, and the qualitative superiority of the Hill fit over the Langmuir isotherm to our data (Fig. S3), we fit our binding data to the Hill isotherm in Eq. 17. We fixed the cooperativity exponent $n = 2$ to ensure standardization between samples and to avoid overfitting the data. While we acknowledge that other cooperative effects may have influenced the shape of the binding isotherm, such as cholesterol-IgG complexes inserting into the bilayer, we consistently observed cooperative behavior across all antigen probes, including DOPE-biotin, from which we expect negligible unbinding into the bulk [13]. Furthermore, we use K_{D}^2 as the fitting parameter in the Hill isotherm, conserving the dimensionality of K_{D} from the thermodynamic definition of equilibrium for a single particle binding to a surface [14]. We further normalize all dissociation constants by the bare surface value: $K_{\text{D}}/K_{\text{D},0}$, reducing the impact of the exact isotherm used.

As shown in Fig. S3B, the precise form of the isotherm does not affect the result in the main text.

Cholesterol sensors slightly favor liquid-disordered domains

We imaged GUVs via epifluorescence microscopy, with 2:2:1 DOPC:DPPC:cholesterol, along with DOPE-rhodamine (0.1%), and cholesterol-PEG0.5k-FITC sensors. The DOPE-rhodamine strongly partitioned into the Ld phase, allowing Ld to be differentiated from Lo. In figure S4 the cholesterol-PEG sensors display a slight preference for the Ld phase over the Lo phase. We hypothesize that the PEG chains disrupt the packing order of the cholesterol, thus causing the sensors to favor Ld while unfunctionalized cholesterol would favor Lo [15]. Thus, the crowding measurements with the cholesterol-PEG0.5k-FITC sensors on HeLa and T47D cells are biased

toward the liquid disordered, non-raft phase, but still measure considerable binding in the raft phase.

Sensors and antibodies approach equilibrium within an hour

To check that our molecular probes reached equilibrium during the incubation time provided, we measured the intensity of both cholesterol-PEG0.5k-FITC sensors and α CD47 antibodies on red blood cells as a function of time, using a flow cytometer. Fig. S5 shows the increase of IgG and cholesterol-PEG0.5k-FITC signal over one hour, for cells incubated in 100 nM cholesterol and 0.25 μ g/mL α CD47 IgG. In our experiments, lipid bilayers were incubated in cholesterol sensors for 30 minutes, ensuring that the sensors reached equilibrium (Fig. S5A). Beads and cells were also incubated in IgG for 30 minutes before collecting image intensity data to find K_D . Fig. S5B suggests that IgG takes approximately one hour to fully reach equilibrium in a flow cytometer. In our experiments, however, we qualitatively found that when allowed to sediment under gravity in the imaging chamber, and particularly when subjected to light pipette mixing, beads and cells reached equilibrium much more quickly. We thus infer that IgG binding kinetics are transport-limited, and that due to the advection introduced by mixing and settling under gravity, our beads and red blood cells were approximately equilibrated. Mammalian cells were incubated in IgG for one hour, ensuring equilibration.

MD Simulation Details

Coarse-grained model

The prepared systems are described using the overdamped Langevin equations of motion, also known as Brownian dynamics, where the velocity $\dot{\mathbf{x}}_i = \mathbf{F}_i/\gamma_i$ of particle i is numerically integrated forward in time and \mathbf{F}_i is the sum of all forces on particle i . All simulations were performed using the GPU-enabled HOOMD-blue simulation package [16].

We coarse-grain (CG) PEG molecules as Kremer-Grest bead-spring polymer chains according to [17], where each CG bead represents the C-O-C monomer unit with length $\sigma = 0.33$ nm. Although our coarse-graining is at an atomic scale, we will still assume an implicit solvent in this simplified model and neglect any polymer interactions with the surrounding solvent molecules.

Non-bonded interactions between monomer pairs are modeled via a purely repulsive Weeks-Chandler-Anderson (WCA) potential

$$V_{\text{WCA}}(\mathbf{r}) = \begin{cases} 0 & \text{if } |r| \geq 2^{1/6}\sigma \\ 4\epsilon \left(\left(\frac{\sigma}{|r|} \right)^{12} - \left(\frac{\sigma}{|r|} \right)^6 \right) & \text{if } |r| < 2^{1/6}\sigma \end{cases} \quad (20)$$

where we set $\epsilon = k_B T$.

Bonded monomers along the polymer chain interact through the “finite extensible nonlinear elastic” (FENE) potential:

$$V_{\text{FENE}}(\mathbf{r}) = \frac{1}{2}kr_0^2 \ln \left(1 - \left(\frac{\mathbf{r}}{r_0} \right)^2 \right) + V_{\text{WCA}}(\mathbf{r}). \quad (21)$$

Additionally, the flexibility of polymer chains is represented using a harmonic bending potential:

$$V_{\text{harm}}(\theta) = \frac{l_p}{2l_b}(\theta - \theta_0)^2 \quad (22)$$

where θ is the angle between three monomers along a chain. We choose the persistence length $l_p = 1\sigma$ and equilibrium bond length as $l_b = \sigma$.

All surface polymers are tethered using two wall-potentials V_{wall} which constrains the vertical position of the first monomer, similar to MD methods in [18].

Antibodies interact through a similar WCA potential with PEG monomers:

$$V_{\text{WCA}}(\mathbf{r}) = \begin{cases} 0 & \text{if } |r| \geq 2^{1/6}r_a \\ 4\epsilon \left(\left(\frac{r_a}{|r|} \right)^{12} - \left(\frac{r_a}{|r|} \right)^6 \right) & \text{if } |r| < 2^{1/6}r_a \end{cases} \quad (23)$$

where the equilibrium distance is $r_a = (\sigma + d_a)/2$ where d_a is the coarse-grained antibody diameter.

Average sensor height

We simulated sensor polymers at a surface density of $1000/\mu\text{m}^2$, in agreement with the experimental coverage of PEG-FITC conjugates on silica beads.

The degree of polymerization was varied from $N = 10$ to $N = 200$ to span the range of polymer contour lengths between PEG0.5k and PEG10k. After an initial equilibration period, we track the vertical height z of the end monomer above the surface, which corresponds to the location of the FITC sensor. The monomer hard sphere radius $r_{\text{HS}} = 2^{1/6}(\sigma/2)$ was subtracted from z since the hard sphere bead never overlaps with the underlying surface. The spatial data were binned and averaged to compute the probability distribution $P(z)$ of sensor positions for various polymer linker lengths. The relationship between N and $\langle h \rangle$ is observed to follow $\langle h \rangle \sim N^{3/5}$, in agreement with Flory theory of a mushroom brush (Fig. S6). This result is expected given the diluteness of the polymer sensors on the surface.

Antibody insertion into PEG brush

We simulate free antibody with PEG2k polymers with $N = 45$ tethered to the cell surface at a surface density of $30000/\mu\text{m}^2$. After equilibration, the center of mass position of the antibody was binned as a function of height above the surface, and the hard sphere radius of the antibody was again subtracted such that $z = 0$ indicates antibodies that are flush with the cell surface. The size of an IgG antibody is ≈ 10 nm [19, 20], which is larger than the PEG2k brush size of $\approx 2 - 3$ nm. We assume that only the Fab region sticks into the PEG2k brush. Therefore, we modeled only the Fab region of the IgG with 4 nm spherical particles, which also recovered the experimentally observed brush potential of $\Delta U = 1k_{\text{B}}T$ at the surface. To obtain the effective brush crowding potential $\langle \Delta U \rangle$, numerical integration of Eq. 11 was performed and normalized by the effective potential of the PEG0.5k sensor.

Coarse graining RBC proteins

Based on proteomics literature, we model the RBC cell surface as a bidisperse polymer brush consisting of the two most abundant proteins based on extracellular size and surface density, GYPA and Band 3 (Fig. S7). We choose the coarse-grained bead diameter of GYPA to be 4 nm, representing the 4-sugar side chain, and use $N = 7$ beads to maintain the contour length of GYPA to be roughly 28 nm. For Band 3, we coarse-grain the branched N-glycan on the extracellular domain into a single chain with 2 nm beads while choosing $N = 10$ to maintain the ≈ 20 nm contour length. Since the RBC surface proteins are taller than the size of an IgG, we assume that the whole IgG interacts with the glycocalyx. Therefore, we modeled the IgG with 11 nm spherical particles, which recovered a repulsive penalty of $\Delta U = 2k_{\text{B}}T$ at the surface, which is reasonable since the RBC brush is taller than the PEG brush and the bulk size of the antibody will dictate the repulsive potential. The effective brush potential $\langle \Delta U \rangle$ was then obtained similarly as in the PEG brush simulations.

Materials

1,2-dioleoyl-sn-glycero-3-phosphocholine (DOPC, 850375C), 1,2-dioleoyl-sn-glycero-3-phosphoethanolamine-N-[methoxy(polyethylene glycol)-2000] (18:1 PEG2k PE, 880130C), 1,2-dioleoyl-sn-glycero-3-phosphoethanolamine-N-(cap biotinyl) (18:1 biotinyl cap PE, 870273C), and 1,2-dipalmitoyl-sn-glycero-3-phosphocholine (DPPC, 850355C) in chloroform and 1,2-dipalmitoyl-sn-glycero-3-phosphoethanolamine-N-(cap biotinyl) (16:0 biotinyl cap PE, 870277P) in solid form, were purchased from Avanti Polar Lipids (Alabaster, AL).

Cholesterol (stabilized with α -Tocopherol, catalog number: C3624, lot number: YB46F-QS) was purchased from TCI chemical.

Monoclonal antibody raised against Fluorescein (1F8-1E4; catalog number: 31242) was purchased from Invitrogen. Alexa Fluor 647 labeled anti-biotin monoclonal antibody (BK-1/39; catalog number: sc-53179 AF647) was purchased from Santa Cruz Biotechnology. Human HER2/ErB2 C-terminal poly-His protein (catalog number: 10004-H08H), Human CD45 C-terminal poly-His protein (extracellular domain; catalog number: 14197-H08H), and anti-HER2 monoclonal antibody (catalog number: 10004-MM03) were purchased from Sino Biological US. Recombinant NS0-derived mouse CD45 protein with C-terminal 6-His tag was purchased from R&D systems (catalog number: 114-CD-050 Lot NHF0318121). Monoclonal antibodies against mouse CD45RB (C363-16A; catalog number: 103311) and pan-CD45 (I3/2.3; catalog number: 147715) were purchased from BioLegend.

Silica microspheres (4.07 μ m; catalog code: SS05002; lot number: 12602) were purchased from Bangs Laboratories.

Cholesterol-PEG-Amine, MW 1k (catalog number: PLS-9961), MW 2k (catalog number: PLS-9962), MW 5k (catalog number: PLS-9964), and MW 10k (catalog number: PLS 9965) were purchased from Creative PEGWorks. NHS-Fluorescein (5/6-carboxyfluorescein succinimidyl ester) (NHS-FITC; catalog number:46409) and Zeba Spin Desalting Columns, 7K MWCO (catalog number: 89882) were purchased from Thermo Scientific.

Alexa Fluor 647 NHS Ester (Succinimidyl Ester) (NHS-AF647; catalog number: A20006), Alexa Fluor 555 NHS Ester (Succinimidyl Ester) (NHS-AF555; catalog number: A20009), and Alexa Fluor 488 NHS Ester (Succinimidyl Ester) (NHS-AF488; catalog number: A20000) were purchased from Invitrogen.

Trypsin-EDTA (0.05%; catalog number: 25300054), High-glucose Dulbecco's Modified Eagle Media (DMEM; catalog number: 10566024), high-glucose Roswell Park Memorial Institute 1640 media (RPMI; catalog number: 61870036), Penicillin-streptomycin (catalog number: 15140122), and fetal bovine serum (FBS; 10437028) were purchased from Gibco.

Single-donor human whole blood (catalog number: IWB1K2E10ML) was purchased from Innovative Research. Blood was de-identified. The researchers involved in this study did not take part in sample collection, and did not have any contact with the donor.

MATLAB educational license was obtained from MathWorks Inc.

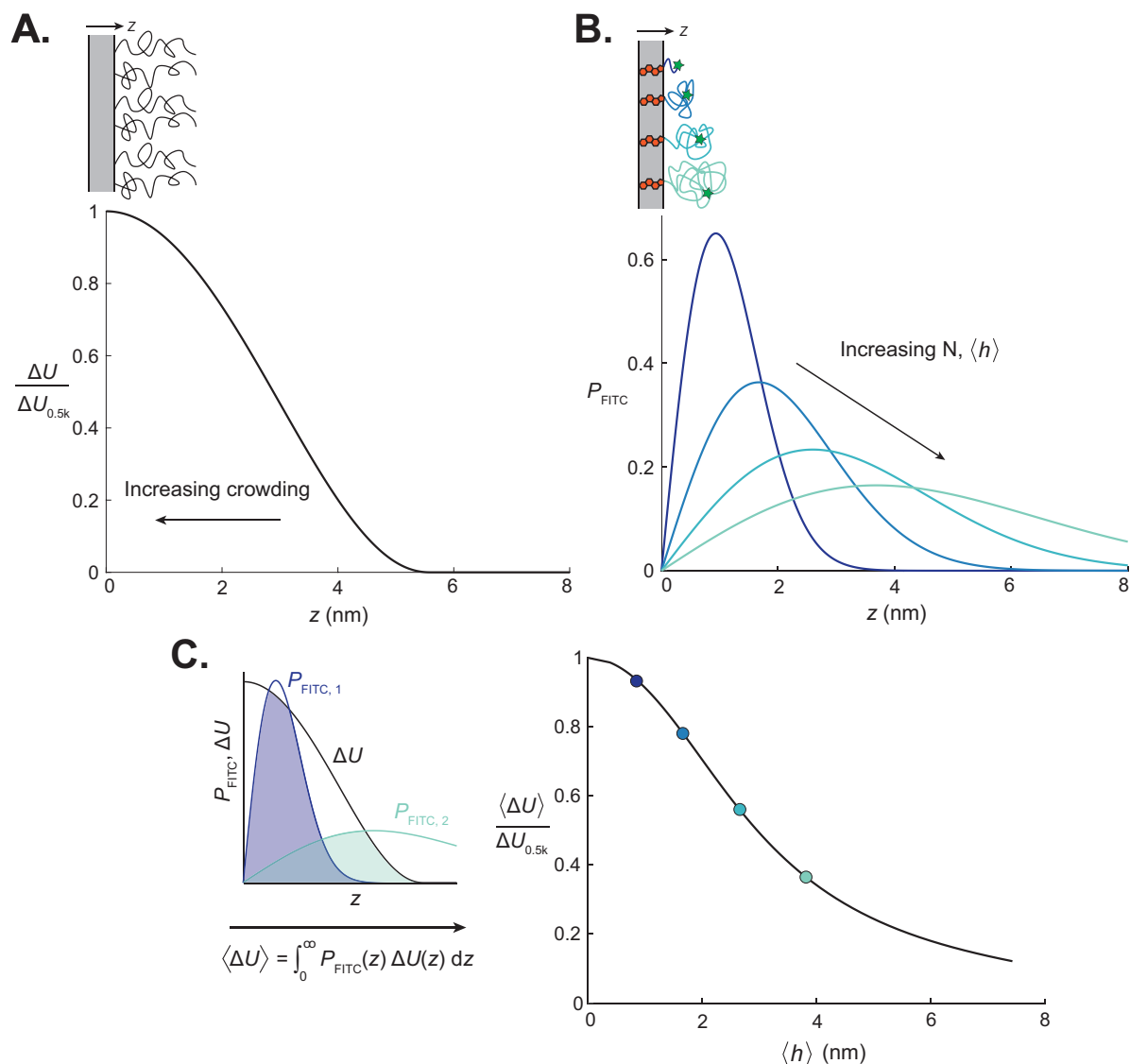


Figure S1: Modeling the crowding landscape experienced by antibodies binding to PEG-tethered FITC antigens in a PEG polymer brush. (A) Repulsive potential ΔU exerted on an adsorbing colloid by a PEG brush with mean height $\langle h \rangle = 3.3\text{nm}$. The repulsive potential varies with distance from the surface z according to the Milner, Witten, and Cates description of monomer density a polymer brush, with the semidilute scaling relationship between osmotic pressure and volume fraction (Eq. 10). The repulsive potential is normalized by the value at the grafting surface, as reported by a PEG0.5k-FITC sensor, $\Delta U_{0.5k}$. (B) End-monomer distribution for surface-tethered polymer mushrooms. Cholesterol-PEG-FITC sensors are modeled as continuous Gaussian chains, with the end monomer, bound to FITC, sampling a distribution of heights P_{FITC} according to Eq. 13. Curves are plotted for sample polymers with $N = 7, 23, 56$, and 113 , with PEG $l = 0.6$ nm. (C) Weighted repulsive potentials account for antigen flexibility and measurement limitations. (Left) Repulsive potentials are weighted by the FITC distribution for each theoretical PEG sensor and integrated across all space to yield a mean potential $\langle \Delta U \rangle$. (Right) Mean potentials are plotted for a series of theoretical sensors, each having a distinct mean height $\langle h \rangle$. Points corresponding to the mean heights of the sample sensors in Fig. S1B are highlighted.

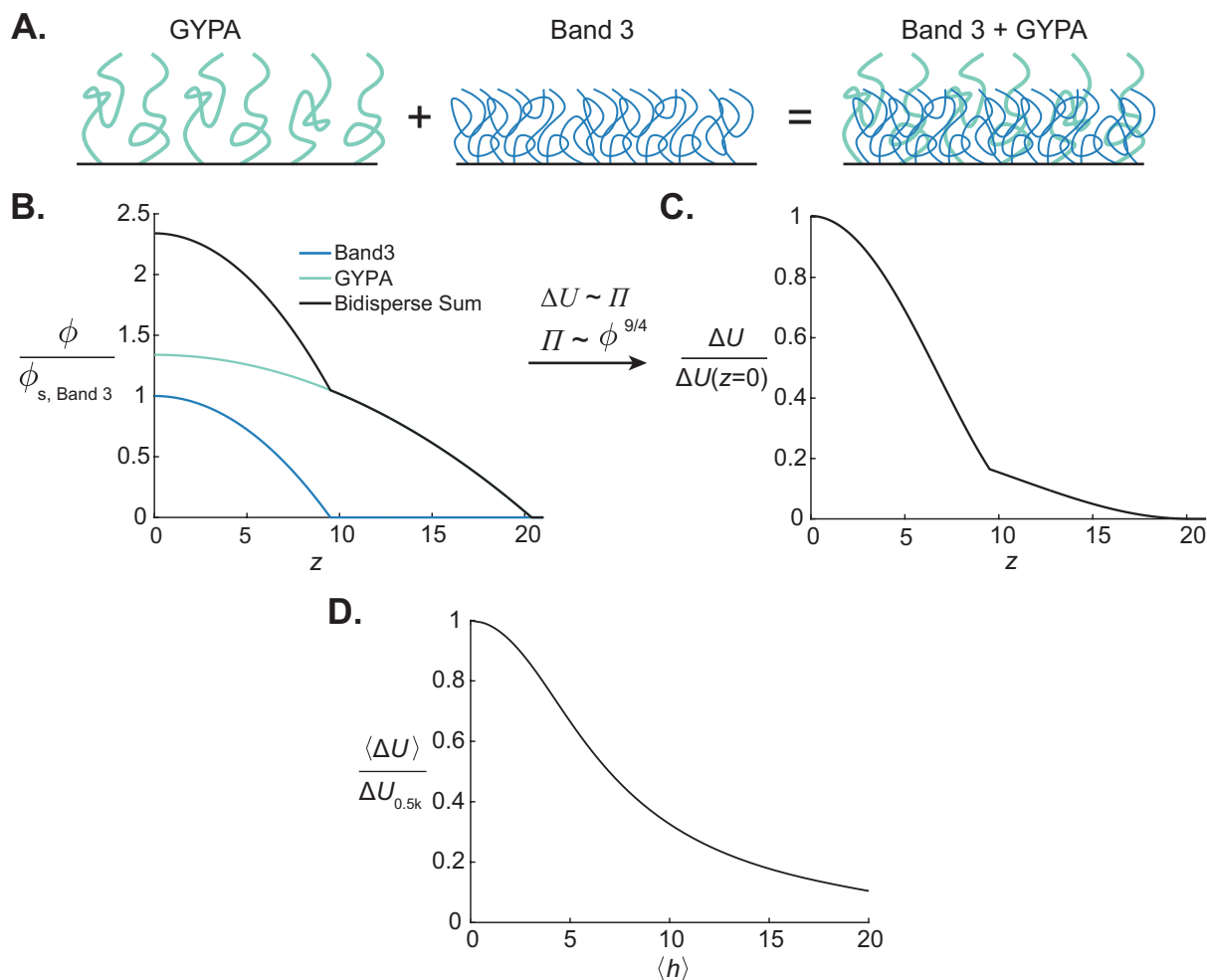


Figure S2: Modeling the red blood cell (RBC) glycocalyx as a bidisperse polymer brush containing glycophorin A (GYPA) and Band 3, using analytical theory. (A) Illustration of the bidisperse polymer brush represented in this analysis. GYPA is taller than Band 3 and has larger monomers but is expressed at a lower density on the RBC surface. Brushes are directly superimposed and assumed to behave independently of one another. (B) Monomer volume fraction distributions according to Eq. 9 are plotted for both GYPA and Band 3 and normalized by the surface volume fraction of Band 3. For each protein, the inputs ϕ_s and L_0 are estimated based on proteomics data and glycosylation characterization. The profiles for the two proteins are superimposed to produce a bidisperse volume fraction profile. (C) Crowding potential of the glycocalyx plotted as a function of height. The monomer density profile in Fig. S2B is converted to a repulsive potential that excludes adsorbing IgG using Eqs. 8 and 5. The potential is normalized against its value at the membrane surface. (D) Mean brush potential experienced by PEG sensors on the RBC surface. The bidisperse polymer brush potential ΔU is weighted by the FITC distribution P_{FITC} from Fig. S1B for a series of sensors, according to Eq. 11. The resulting mean potential $\langle \Delta U \rangle$ is plotted as a function of mean sensor height $\langle h \rangle$

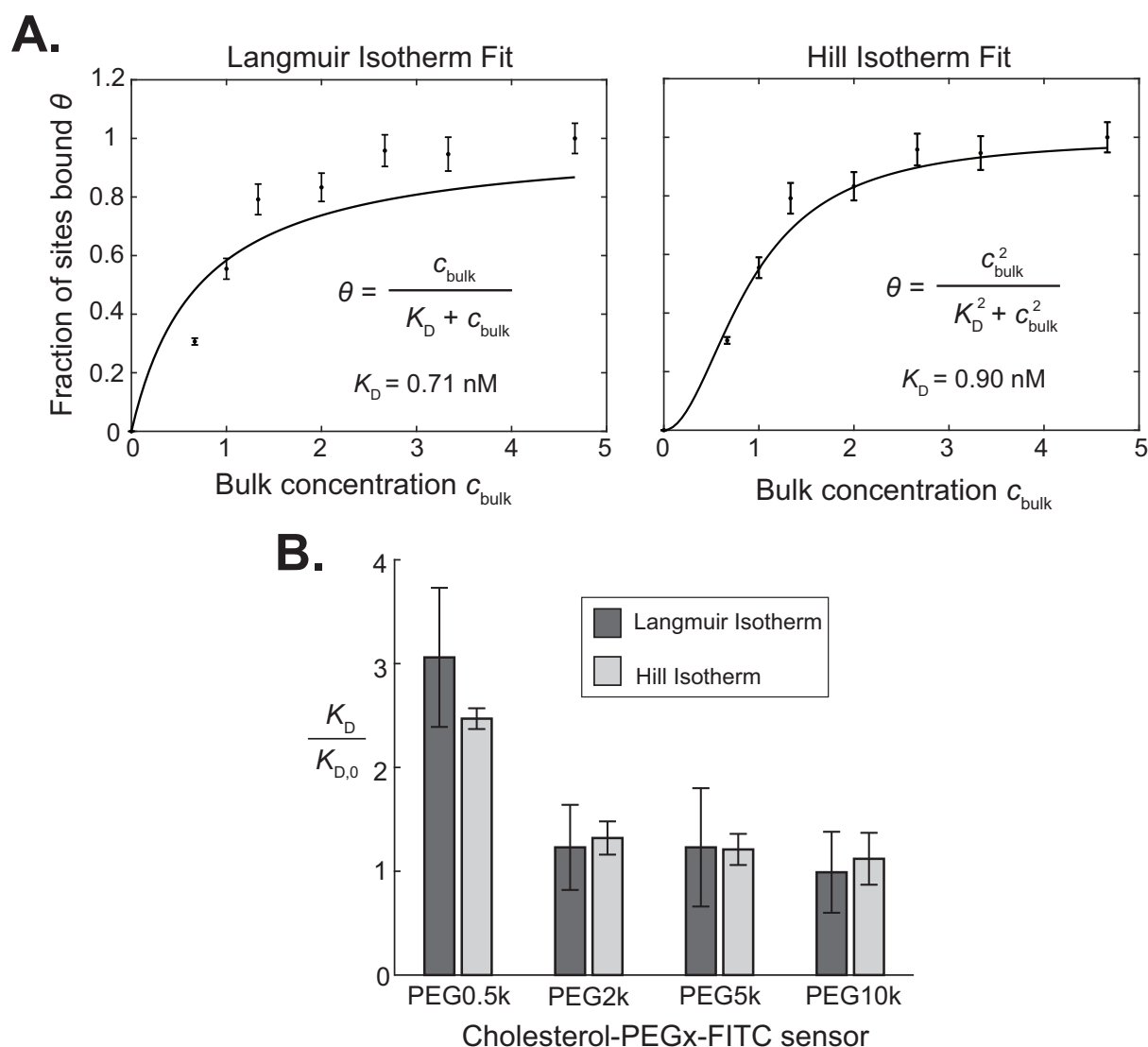
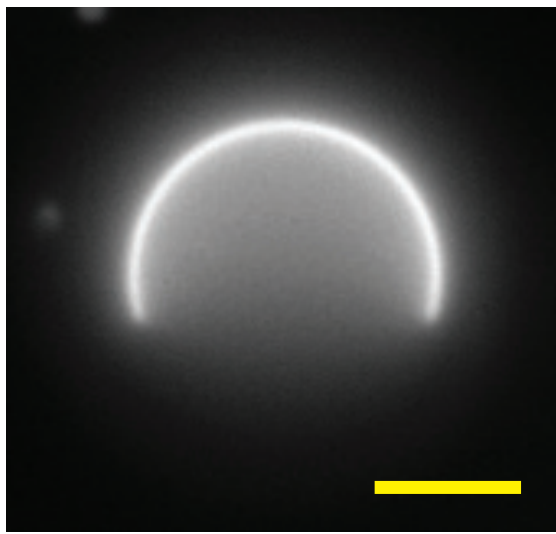
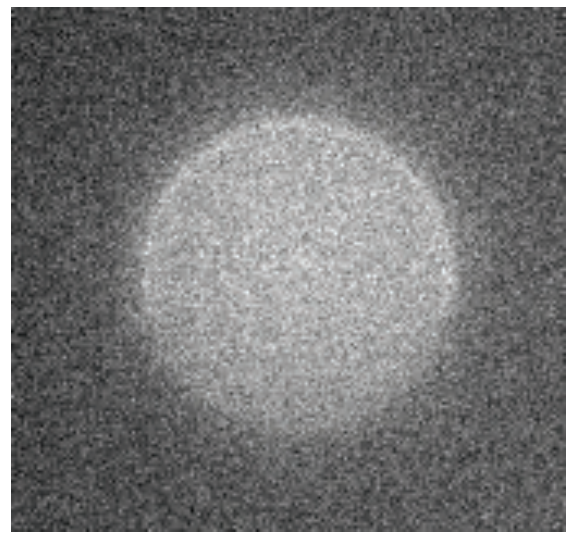


Figure S3: A comparison of Langmuir isotherm and Hill isotherm fits to antibody binding data shows that the fitting method has little impact on our conclusions. (A) For a cholesterol-PEG0.5k-FITC sensor, the fraction of bound antigen sites, normalized by the concentration of antibodies bound at saturation, is plotted as a function of bulk antibody concentration. (Left) The Langmuir isotherm is fit to the data. (Right) The Hill isotherm with cooperativity coefficient $n = 2$ is fit to the data. (B) For all cholesterol-PEGx-FITC sensors on beads we plot the ratio of K_D with a PEG2k brush blocking binding to $K_{D,0}$ with no brush. Dissociation constants were fitted to binding data with both the Langmuir isotherm and Hill isotherm. For all sensors, the ratio of dissociation constants varies by approximately 15% or less, with no significant qualitative difference in the overall trend.



DOPE-rhod (Ld)



Chol-PEG0.5k-FITC

Figure S4: The 555 nm DOPE-rhodamine channel is shown on the left, with the Ld phase of a GUV appearing as a bright crescent. The 488 nm cholesterol-PEG-FITC channel is shown on the right, with a slightly brighter half aligning with the rhodamine channel. Scale bar is 5 μm .

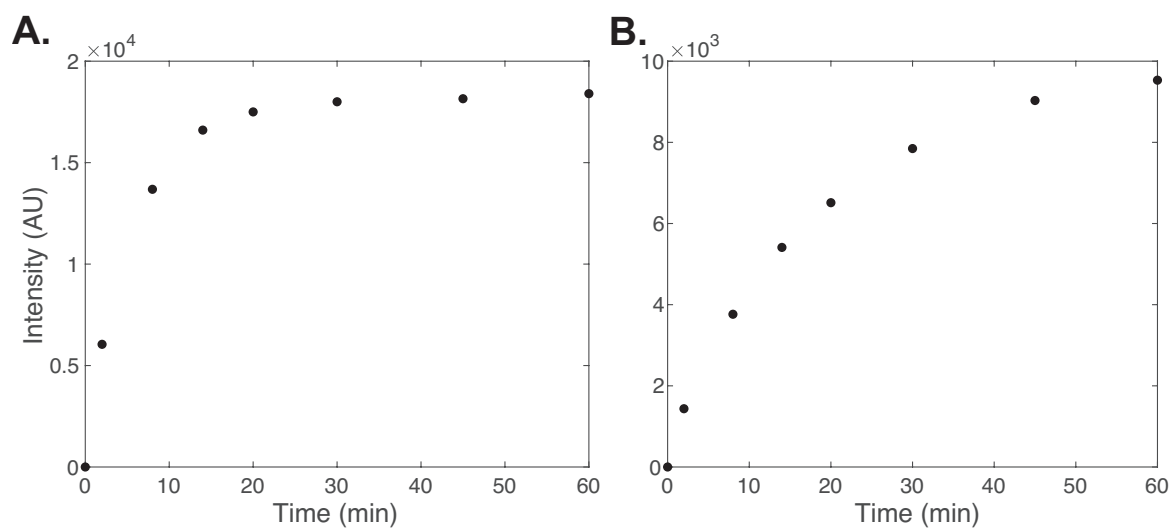


Figure S5: Kinetics of sensor and IgG binding to red blood cells. (A) Red blood cells were incubated in 100 nM cholesterol-PEG0.5k-FITC sensors and the FITC fluorescence intensities measured using flow cytometry. Intensities are plotted as a function of time. (B) Red blood cells were incubated in 0.25 $\mu\text{g}/\text{mL}$ αCD47 IgG antibody labeled with Alexa Fluor 647 and the antibody fluorescence intensities plotted as a function of time.

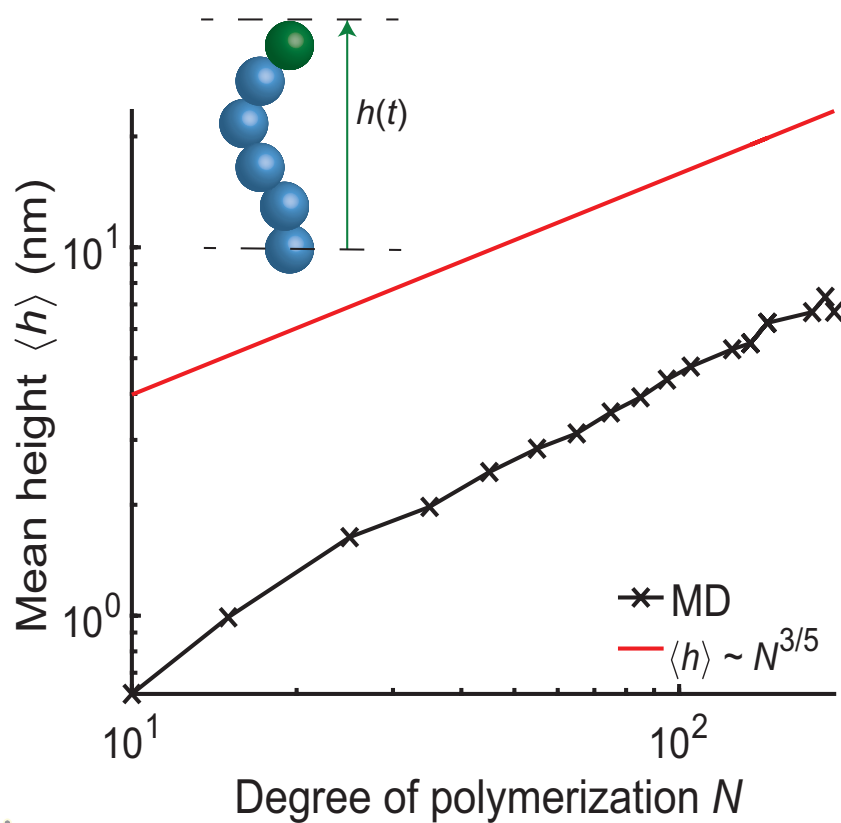


Figure S6: MD simulation of average height of FITC sensor. The average height of the FITC sensor (green) was obtained for various polymer degrees of polymerization, which is controlled by tuning the number of linker monomers (blue). The red theory line corresponds to a self-avoiding swollen polymer chain in a good solvent.

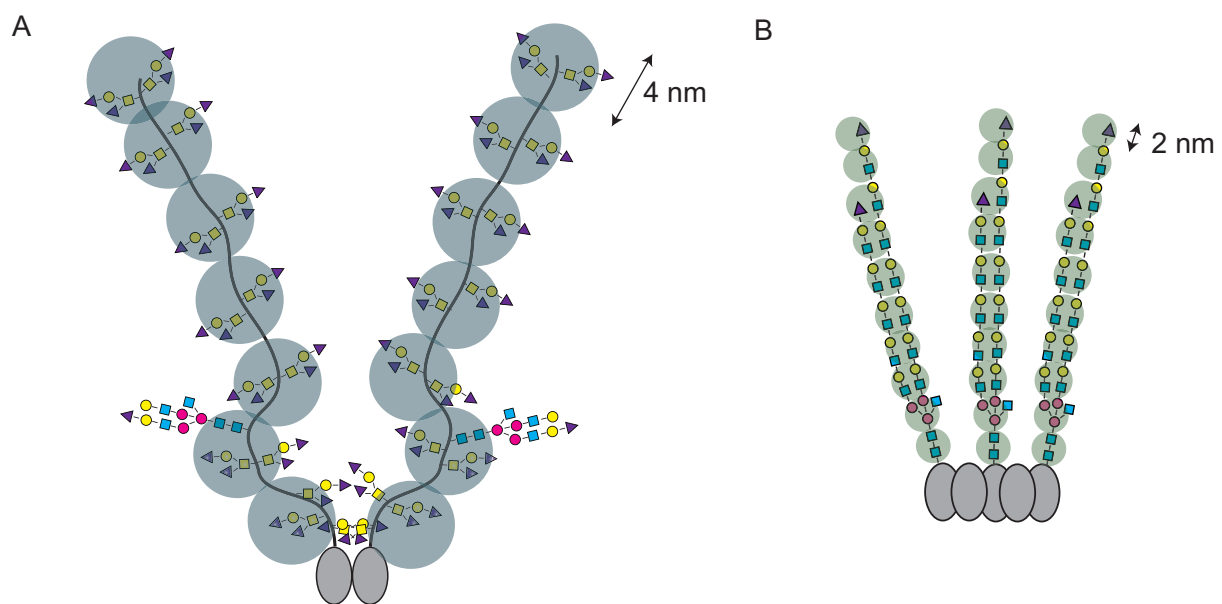


Figure S7: Coarse-graining of Glycophorin A (GYPA) and Band 3 on RBC glycolyx. (A) In the molecular dynamics (MD) simulations, the extracellular domain of GYPA is modeled as two seven-bead polymer chains with bead diameter of 4 nm corresponding to the length of the sugar side chains. (B) Band 3 is modeled as three ten-bead polymer chains with bead diameter of 2 nm corresponding to a pair of sugars across the two side branches [6].

Movie Legends

Movie S1. MD simulation of FITC sensors

MD simulation of FITC sensor (green) with 64 linker monomer units (blue), each of diameter 0.33 nm. Sensors were tethered to the bottom of the simulation box at a surface density of $1000/\mu\text{m}^2$.

Movie S2. MD simulations of antibodies in monodisperse PEG surface

MD simulation of ideal gas antibodies (red) of diameter 4 nm and $N = 45$ PEG brush (grey) with monomer diameter 0.33 nm and surface density of $30000/\mu\text{m}^2$.

Movie S3. MD simulation of antibodies in bidisperse red blood cell surface

MD simulation of ideal gas antibodies (red) of diameter 11 nm in the presence of a bidisperse brush. Glycophorin A (dark green) is represented as a 7 bead chain with monomer diameter 2 nm and surface density of $1300/\mu\text{m}^2$, while Band 3 (light green) is represented as a 10 bead chain with monomer diameter 1 nm and surface density of $6700/\mu\text{m}^2$.

References

- (1) Louis, A. A.; Bolhuis, P. G.; Meijer, E. J.; Hansen, J. P. *The Journal of Chemical Physics* **2002**, *116*, 10547–10556.
- (2) Rubinstein, M.; Colby, R., *Polymer Physics*, 1st ed.; Oxford University Press: 2003.
- (3) Halperin, A. *Langmuir* **1999**, *15*, 2525–2533.
- (4) Milner, S. T.; Witten, T. A.; Cates, M. E. *Macromolecules* **1988**, *21*, 2610–2619.
- (5) Russel, W. B.; Saville, D. A.; Schowalter, W. R., *Colloidal Dispersions*; Cambridge University Press: 1989.
- (6) Aoki, T. *Membranes* **2017**, *7*, 1–19.
- (7) Bryk, A. H.; Wiśniewski, J. R. *Journal of Proteome Research* **2017**, *16*, 2752–2761.
- (8) Gautier, E. F.; Leduc, M.; Cochet, S.; Bailly, K.; Lacombe, C.; Mohandas, N.; Guillonneau, F.; El Nemer, W.; Mayeux, P. *Blood Advances* **2018**, *2*, 2646–2657.
- (9) Shi, J.; Yang, T.; Kataoka, S.; Zhang, Y.; Diaz, A. J.; Cremer, P. S. *Journal of the American Chemical Society* **2007**, *129*, 5954–5961.
- (10) Yang, T.; Baryshnikova, O. K.; Mao, H.; Holden, M. A.; Cremer, P. S. *Journal of the American Chemical Society* **2003**, *125*, 4779–4784.
- (11) Jung, H.; Robison, A. D.; Cremer, P. S. *Journal of Structural Biology* **2009**, *168*, 90–94.
- (12) Jung, H.; Yang, T.; Lasagna, M. D.; Shi, J.; Reinhart, G. D.; Cremer, P. S. *Biophysical Journal* **2008**, *94*, 3094–3103.
- (13) Delaveris, C. S.; Webster, E. R.; Banik, S. M.; Boxer, S. G.; Bertozzi, C. R. *Proceedings of the National Academy of Sciences of the United States of America* **2020**, *117*, 12643–12650.
- (14) Phillips, R.; Kondev, J.; Thierot, J.; Garcia, H., *Physical Biology of the Cell*, 2nd ed.; Garland Science, Taylor and Francis Group: 2012.
- (15) Veatch, S. L.; Keller, S. L. *Biophysical Journal* **2003**, *85*, 3074–3083.
- (16) Anderson, J. A.; Glaser, J.; Glotzer, S. C. *Computational Materials Science* **2020**, *173*, DOI: 10.1016/j.commatsci.2019.109363.

- (17) Lee, H.; De Vries, A. H.; Marrink, S. J.; Pastor, R. W. *Journal of Physical Chemistry B* **2009**, *113*, 13186–13194.
- (18) Son, S.; Takatori, S. C.; Belardi, B.; Podolski, M.; Bakalara, M. H.; Fletcher, D. A.; Fletcher, D. A.; Fletcher, D. A. *Proceedings of the National Academy of Sciences of the United States of America* **2020**, *117*, 14209–14219.
- (19) De Michele, C.; De Los Rios, P.; Foffi, G.; Piazza, F. *PLoS Computational Biology* **2016**, *12*, 1–17.
- (20) Tan, Y. H.; Liu, M.; Nolting, B.; Go, J. G.; Gervay-Hague, J.; Liu, G.-y. *ACS Nano* **2008**, *2*, 2374–2384.